

GenCast: Diffusion-based ensemble forecasting for medium-range weather

Ilan Price^{*,1}, Alvaro Sanchez-Gonzalez^{*,1}, Ferran Alet¹, Timo Ewalds¹, Andrew El-Kadi², Jacklynn Stott¹, Shakir Mohamed¹, Peter Battaglia¹, Remi Lam¹ and Matthew Willson¹

^{*}Equal contributions, ¹Google DeepMind, ²Imperial College, London

Probabilistic weather forecasting is critical for decision-making in high-impact domains such as flood forecasting, energy system planning or transportation routing, where quantifying the uncertainty of a forecast—including probabilities of extreme events—is essential to guide important cost-benefit trade-offs and mitigation measures. Traditional probabilistic approaches rely on producing ensembles from physics-based models, which sample from a joint distribution over spatio-temporally coherent weather trajectories, but are expensive to run. An efficient alternative is to use a machine learning (ML) forecast model to generate the ensemble, however state-of-the-art ML forecast models for medium-range weather are largely trained to produce deterministic forecasts which minimise mean-squared-error. Despite improving skills scores, they lack physical consistency, a limitation that grows at longer lead times and impacts their ability to characterize the joint distribution. We introduce GenCast, a ML-based generative model for ensemble weather forecasting, trained from reanalysis data. It forecasts ensembles of trajectories for 84 weather variables, for up to 15 days at 1° resolution globally, taking around a minute per ensemble member on a single Cloud TPU v4 device. We show that GenCast is more skillful than ENS, a top operational ensemble forecast, for more than 96% of all 1320 verification targets on CRPS and Ensemble-Mean RMSE, while maintaining good reliability and physically consistent power spectra. Together our results demonstrate that ML-based probabilistic weather forecasting can now outperform traditional ensemble systems at 1°, opening new doors to skillful, fast weather forecasts that are useful in key applications.

1. Introduction

Individually and collectively, we rely on accurate weather forecasts to plan ahead—whether to carry an umbrella, how to route an aeroplane, or even how to optimize the use of renewable energy in a power grid. Forecasts are not always accurate however, and to make effective decisions, one needs to understand how certain a forecast is. While the weather is highly predictable in some circumstances, in others the butterfly effect can result in a rapid growth in forecast error (Edward, 1993). This need to understand predictability (Kalnay, 2003; Palmer and Hagedorn, 2006) has motivated a paradigm shift: over the past 30 years weather agencies have transitioned away from purely deterministic forecast systems—which focus on the accuracy of a single best guess of the upcoming weather—to generating ensembles of forecasts stochastically, which approximate samples from the distribution over future weather scenarios (ECMWF, 2019; Palmer, 2019; Roberts et al., 2023; Yamaguchi et al., 2018; Zhu et al., 2012b). These ensembles are based on Numerical Weather Prediction (NWP), and constitute essential tools across many sectors. Nonetheless, they still exhibit biases and errors, and are very computationally expensive to generate. This limits the number of ensemble members that can feasibly be generated, and consequently limits the ability of the ensembles to capture the tails of the weather distribution.

In recent years the machine learning (ML) community has made rapid progress in exceeding the skill and speed of traditional NWP forecast models on medium-range forecasting (Bi et al., 2022,

2023; Chen et al., 2023; Kurth et al., 2022; Lam et al., 2022, 2023; Li et al., 2023a; Nguyen et al., 2023). However the focus has largely been on deterministic forecasting and the minimization of root-mean-squared error (RMSE), with relatively little emphasis on uncertainty quantification or probabilistic modelling more broadly. Models trained to minimize RMSE will tend to produce blurry forecasts at longer lead times, which are closer to an ensemble mean than to a deterministic NWP forecast (Lam et al., 2023). While these models have been used together with ad-hoc perturbations to produce ensembles (Bi et al., 2022; Kurth et al., 2022; Li et al., 2023a), their ensembles inherit the issue of blurring, and have not been as successful at matching the skill and reliability of NWP ensembles as their deterministic counterparts have been in surpassing the skill of a deterministic NWP forecast.

In this paper, we introduce a novel ML-based approach for probabilistic weather forecasting—called GenCast—which generates global, 15-day ensemble forecasts that are more accurate than the top operational ensemble forecast, the European Centre for Medium-range Weather Forecasts (ECMWF)’s ENS, in a fraction of the time. GenCast implicitly models the joint probability distribution of the weather state over space and time, operating on a 1° latitude-longitude grid, on 12 hour time steps, and representing 6 surface variables, and 6 atmospheric variables at 13 vertical pressure levels. It is a diffusion model (Karras et al., 2022; Sohl-Dickstein et al., 2015), and it leverages a neural network architecture closely related to that of GraphCast (Lam et al., 2023), with the notable difference that the Processor component uses a sparse transformer (Vaswani et al., 2017) with a different graph connectivity pattern from GraphCast.

GenCast is skillful, fast, and displays good reliability, as well as physically consistent power spectra even at long lead times. It outperforms both ENS and GraphCast-Perturbed—an ensemble variant of a leading deterministic ML forecasting model GraphCast—on all of Ensemble-Mean RMSE, bias, Continuous Ranked Probability Score (CRPS), and Brier scores on extreme events. The ensembles it generates exhibit comparable or better reliability than ENS and GraphCast-Perturbed, as measured by rank-histograms and spread-skill scores, and each ensemble member is a spatio-temporally coherent, sharp prediction. It maintains important properties of physically plausible predictions such as an appropriate spherical harmonic power spectrum, addressing one of the primary limitations of ML models like GraphCast-Perturbed which blur at long lead times due to their MSE training objective. GenCast is also extremely computationally efficient relative to traditional NWP models, generating each 15-day weather trajectory in around a minute on a single Cloud TPU v4 (Jouppi et al., 2023), opening the door to the possibility of generating orders of magnitude larger ensembles in future.

2. Related work

In the past few years, there has been a rapid increase in the number of ML-based global weather forecasting models that operate at 1.5° resolution or finer as alternatives to purely NWP-based methods, enabled and accelerated by work on benchmarking by Rasp et al. (2020, 2023). Multiple models now outperform top deterministic operational forecasts.

KeislerNet (Keisler, 2022) was a deterministic model operating on 1° latitude-longitude resolution with competitive performance versus ECMWF’s HRES, and the National Oceanic and Atmospheric Administration (NOAA)’s Global Forecasting System (GFS), both state-of-the-art deterministic NWP forecasts. FourCastNet (Kurth et al., 2022; Pathak et al., 2022) was the first global 0.25° model and also showed competitive performance versus HRES on a number of variables. Pangu-Weather (Bi et al., 2022, 2023) also operated on 0.25° and 7-day lead times. It outperformed HRES on a number of variables, and demonstrated promising results on probabilistic metrics using perturbed initial conditions. GraphCast (Lam et al., 2022, 2023) operated on 0.25° , 37 vertical levels, and 10-day lead

times, and was the first to definitively outperform HRES. FengWu (Chen et al., 2023) demonstrated competitive performance with GraphCast, with an emphasis on longer lead-time RMSE scores using a novel replay buffer technique.

Stormer (Nguyen et al., 2023) presents a further deterministic model which operates at 1.4° resolution, outperforming HRES and GraphCast on RMSE at this lower resolution, and proving competitive with ECMWF’s ENS ensemble forecast mean on RMSE up to approximately 5 days. FuXi’s (Li et al., 2023a) ensemble variant shows competitive performance with ENS on RMSE of the ensemble mean and CRPS at 0.25° up to approximately 7 days, after which ENS is better, though the model exhibits significant under-dispersion and smoothing at lead times of longer than 5 days. Neural GCM (Kochkov et al., 2023) developed a hybrid ML-NWP model, which incorporates a neural network subgrid model into a differentiable global circulation model, which is trained end to end. It operates at 0.7° for deterministic forecasts and 1.4° for ensemble forecasts, showing competitive performance with ENS.

Beyond global medium range weather forecasting, there has also been work on using ML models to tackle related problems like short-term regional probabilistic forecasting (Andrychowicz et al., 2023; Ravuri et al., 2021; Zhang et al., 2023), ensemble emulation (Li et al., 2023b), and applying diffusion models to tasks like precipitation nowcasting (Asperti et al., 2023; Gao et al., 2023) and turbulent flow simulation (Kohl et al., 2023). Outside of weather, diffusion models have been applied to multivariate time series (Rasul et al., 2021) and to spatio-temporal data including videos (Blattmann et al., 2023; Harvey et al., 2022; Ho et al., 2022a,b; Yang et al., 2023) and spatio-temporal graphs (Hu et al., 2023; Wen et al., 2023).

3. Methods

3.1. Task definition and general approach

Our goal is to draw samples from the joint probability distribution, $p(X^{1:T}|O)$, over T -step forecasts $X^{1:T}$ conditional on observations O made during a time window that leads up to (and perhaps slightly beyond) the initialisation time $t = 0$. Each X^t represents 6 atmospheric variables at 13 vertical pressure levels and 6 surface variables (see Table A.1), at each point on a 1° latitude-longitude grid, at timestep t . The time interval between successive states, X^t and X^{t+1} is 12 hours, and the forecast horizon we evaluate is 15 days, i.e., $T = 30$.

Subject to some conditional independence assumptions (see Appendix A.1), we consider a factorised distribution such that the next state is conditioned only on the two previous states

$$p(X^{-1:T}|O) = p(X^{-1:0}|O) \prod_{t=1}^T p(X^t|X^{t-2:t-1}). \quad (1)$$

We do not directly condition on observations, O . Instead, to approximate sampling from $p(X^{-1:0}|O)$ we use an ensemble of NWP-based analysis¹ states based on ECMWF’s ERA5 archive of reanalysis data (Hersbach et al., 2020), including the ERA5 EDA (ensemble of data assimilations). Details are in Section 4.2 and Appendix A.4.

To sample a forecast trajectory $X^{1:T}$, we first sample initial conditions $X^{-1:0}$ based on NWP analysis, then for each $t \in 1:T$ we sample X^t auto-regressively conditional on the previous two steps $X^{t-2:t-1}$. Multiple samples of $X^{1:T}$ can then be used to compute Monte-Carlo estimates of any probabilities

¹‘Analysis’ refers to an estimate of the state of the atmosphere based on observations; ‘reanalysis’ is an analysis computed retrospectively based on historical observations.

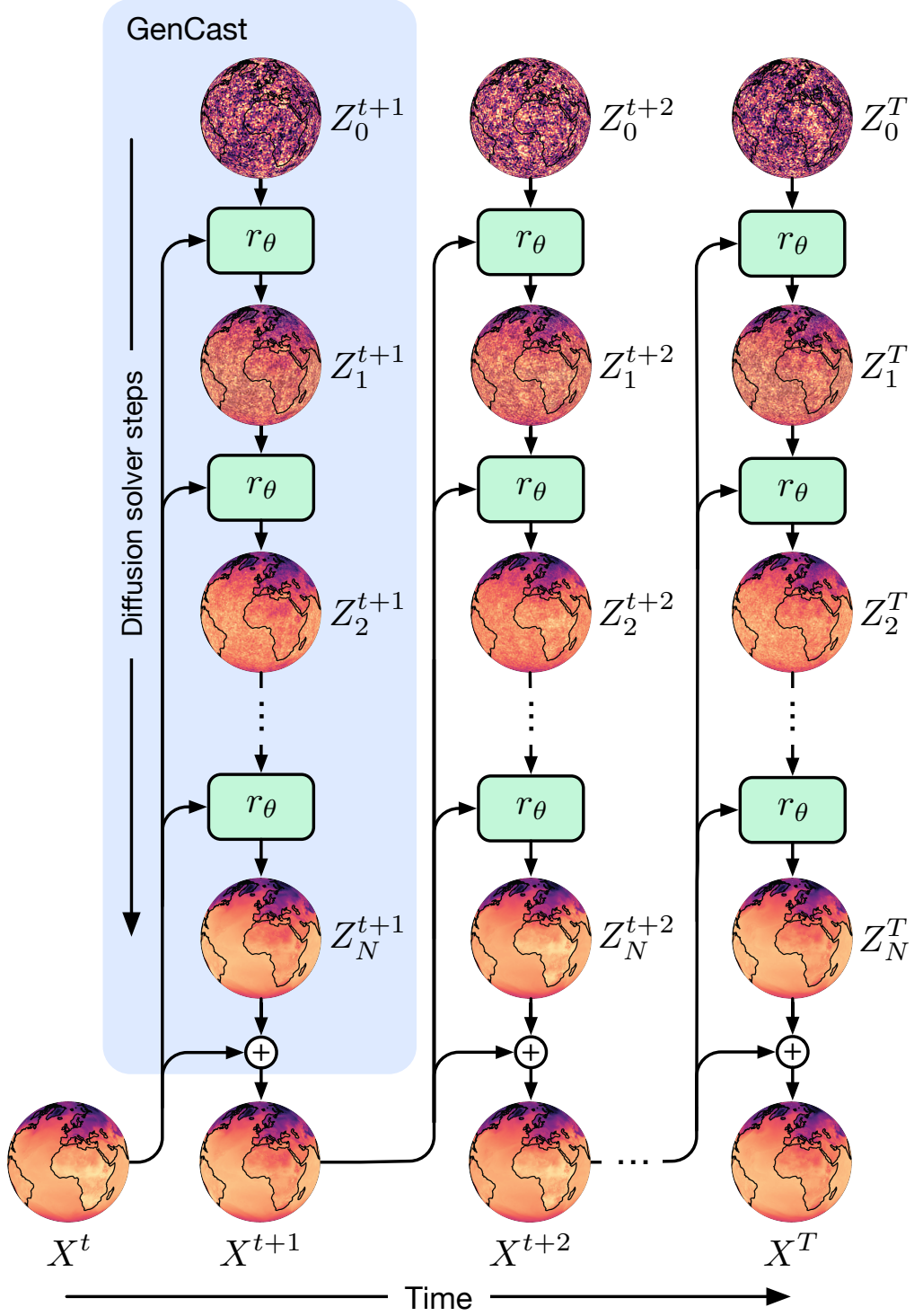


Figure 1 | Schematic of GenCast. A future atmospheric state X^{t+1} is produced by iteratively refining a candidate state initialized purely from noise, conditioned on the previous two atmospheric states (X^{t-1} and X^t), though for simplicity the schematic only shows conditioning on the previous atmospheric state. Each refinement iteration is performed by taking a solver step r_θ (see Section 3.2.1). Once the future state is produced then the process can be repeated autoregressively to produce subsequent future atmospheric states X^{t+2}, \dots, X^{t+T} . Because the refinement process is initialised with noise, the whole process can be repeated more than once, each time starting from a different noise sample, to generate an ensemble of trajectories that contain information about the distribution of possible future states.

or expectations of interest. This is a form of ensemble forecasting, which is a popular method in traditional NWP-based forecasting, because the joint distribution is extremely high-dimensional and is thus intractable to represent explicitly. Unlike traditional approaches, however, which use initial conditions derived from NWP-based analysis states to initialize an NWP forecast, in this work we instead use these initial conditions to seed a learned forecast model.

3.2. Diffusion model specification

Our key innovation is to model $p(X^t|X^{t-2:t-1})$ with a learned neural network-based diffusion model that allows us to draw samples from the distribution. Rather than sampling X^t directly, our approach is to sample residuals Z^t with respect to the most recent weather state X^{t-1} , which have been normalized to unit variance on a per-variable and per-level basis as was done for GraphCast in [Lam et al. \(2023\)](#). X^t is then recovered as $X^t = X^{t-1} + SZ^t$, where S is a diagonal matrix which inverts the normalization².

As background, diffusion models ([Karras et al., 2022](#); [Sohl-Dickstein et al., 2015](#); [Song et al., 2021](#)) are a family of generative ML models used to generate new samples from a given data distribution. The generation process begins by sampling from a prescribed noise distribution—typically an i.i.d. Gaussian distribution—and then iteratively transforming that sample using a learned denoiser, until it approximates a sample from the target distribution. At each step in this process, the transformed datapoint is a sample from one of a continuous family of distributions parameterised by a noise level σ , which interpolate between the noise and data distributions. The denoiser model used in this data generation process is trained by adding varying amounts of noise to the training data, tasking the model with denoising the noisy data, and minimising the mean squared error.

We broadly follow the diffusion framework presented in [Karras et al. \(2022\)](#), and refer the reader to their paper for a more rigorous introduction to diffusion, as well as a detailed treatment of the available modelling decisions. We adopt their choices of noise schedule, noise scaling, loss weighting by noise level, and preconditioning. However we make changes to the noise distribution, the training-time distribution of noise levels, and add additional loss weightings, all of which are described below. These changes improve performance on the task of probabilistic weather forecasting.

3.2.1. Sampling process

The sampling process begins by drawing an initial sample Z_0^t from a noise distribution on the sphere $p_{\text{noise}}(\cdot|\sigma_0)$ that is described in Section 3.2.2, at a high initial noise level σ_0 . After N steps of transformation we end up at $Z_N^t := Z^t$, our sample from the target distribution at noise level $\sigma_N = 0$. To take us from one to the other, we apply an ODE solver to the probability flow ODE described by [Karras et al. \(2022\)](#); [Song et al. \(2021\)](#). Each step of this solver is denoted by r_θ (see Figure 1), with

$$Z_{i+1}^t = r_\theta(Z_i^t, X^{t-2:t-1}, \sigma_{i+1}, \sigma_i) \quad (2)$$

taking us from noise level σ_i to the next (lower) noise level σ_{i+1} , conditioned on the previous timesteps $X^{t-2:t-1}$.

We use the second-order DPMSolver++2S solver ([Lu et al., 2022](#)), augmented with the stochastic churn (again making use of p_{noise} from Section 3.2.2) and noise inflation techniques used in [Karras et al. \(2022\)](#) to inject further stochasticity into the sampling process. In conditioning on previous timesteps we follow the Conditional Denoising Estimator approach outlined and motivated by [Batzolis et al. \(2021\)](#).

²An exception to this is precipitation, for which we set $X^t = SZ^t$ without adding the previous state.

Each step r_θ of the solver makes use of a learned denoiser D_θ with parameters θ , described in detail below (Section 3.2.3). We take $N = 20$ solver steps per generated forecast timestep. As we are using a second-order solver, each step r_θ requires two function evaluations of the denoiser D_θ (with the exception of the last step which requires only a single evaluation). This results in 39 function evaluations in total. See Appendix A.3.1 for further details including a full list of sampling hyperparameters.

3.2.2. Noise distribution on the sphere

At the core of a diffusion model is the addition and removal of noise, drawn from some distribution $p_{noise}(\cdot|\sigma)$ parameterized by noise level σ . When using diffusion to generate natural images (Ho et al., 2020), p_{noise} is usually chosen to be i.i.d. Gaussian. However we have found it beneficial to use a noise distribution which better respects the spherical geometry of global weather variables. Rather than sampling i.i.d Gaussian noise on the latitude-longitude grid, we instead sample isotropic Gaussian white noise on the sphere, which is then projected onto the grid. This choice of p_{noise} has the consequence that the noise has a flat spherical harmonic power spectrum in expectation. For motivation and details of these changes, see Appendix A.3.3.

3.2.3. Denoiser architecture

To recap, our diffusion sampling process involves taking multiple solver steps r_θ , and each solver step calls a denoiser D_θ as part of its computation. We parameterise the denoiser D_θ following Karras et al. (2022) as a preconditioned version of a neural network function f_θ .

$$D_\theta(Z_\sigma^t; X^{t-2:t-1}, \sigma) := c_{skip}(\sigma) \cdot Z_\sigma^t + c_{out}(\sigma) \cdot f_\theta(c_{in}(\sigma)Z_\sigma^t; X^{t-2:t-1}, c_{noise}(\sigma)). \quad (3)$$

Here Z_σ^t denotes a noise-corrupted version of the target Z^t at noise level σ , and c_{in} , c_{out} , c_{skip} and c_{noise} are preconditioning functions taken from Table 1 in Karras et al. (2022), with $\sigma_{data} = 1$ due to the normalization of targets.

The architecture used for f_θ is based on the GraphCast architecture described in Lam et al. (2023). To be precise, the Encoder and Decoder architectures stay the same, and those inputs to the encoder corresponding to the previous two timesteps are normalized to zero mean and unit variance in the same way. However, unlike in GraphCast, which uses a similar GNN for the Processor architecture as in the Encoder and Decoder, in GenCast the Processor is a sparse transformer model, which computes something analogous to sliding-window attention on 1D or 2D grids, but operating on a spherical mesh. Unlike the multimesh used in GraphCast, the mesh in GenCast is simply a 5-refined icosahedral mesh as defined in Lam et al. (2023), with 10,242 nodes and 61,440 edges.

The Processor consists of 16 consecutive standard transformer blocks (Nguyen and Salazar, 2019; Vaswani et al., 2017), with feature dimension equal to 512. The 4-head self-attention mechanism in each block is such that each node in the mesh attends to itself and to all other nodes which are within its 16-hop neighbourhood on the mesh.

To condition on prior timesteps $X^{t-1:t}$, we concatenate these along the channel dimension with the input to be denoised, and feed this as input to the model. Conditioning on noise level σ is achieved by replacing all layer-norm layers in the architecture with conditional layer-norm (Chen et al., 2021) layers. We transform log noise levels into a vector of sine/cosine Fourier features at 32 frequencies with base period 16, then pass them through a 2-layer MLP to obtain 16-dimensional noise-level encodings. Each of the conditional layer-norm layers applies a further linear layer to output replacements for the standard scale and offset parameters of layer norm, conditioned on these noise-level encodings.

3.2.4. Training the denoiser

At training time we apply the denoiser to a version of the target Z^t which has been corrupted by adding noise $\epsilon \sim p_{\text{noise}}(\cdot|\sigma)$ at noise level σ :

$$Y^t = D_\theta(Z^t + \epsilon; X^{t-2:t-1}, \sigma). \quad (4)$$

We train its output, denoted Y^t , to predict the expectation of the noise-free target Z^t by minimizing the following mean-squared-error objective weighted per elevation level and by latitude-longitude cell area,

$$\sum_{t \in \mathcal{D}_{\text{train}}} \mathbb{E} \left[\lambda(\sigma) \frac{1}{|G||J|} \sum_{i \in G} \sum_{j \in J} w_j a_i (Y_{i,j}^t - Z_{i,j}^t)^2 \right], \quad (5)$$

where

- t indexes the different timesteps in the training set $\mathcal{D}_{\text{train}}$,
- $j \in J$ indexes the variable, and for atmospheric variables the pressure level, i.e. $J = \{z1000, z850, \dots, 2T, \text{MSL}\}$,
- $i \in G$ indexes the location (latitude and longitude coordinates) in the grid,
- w_j is the per-variable-level loss weight, set as in [Lam et al. \(2023\)](#) with the additional sea surface temperature variable weighted at 0.01.
- a_i is the area of the latitude-longitude grid cell, which varies with latitude, and is normalized to unit mean over the grid,
- $\lambda(\sigma)$ is the per-noise-level loss weight from [Karras et al. \(2022\)](#),
- the expectation is taken over $\sigma \sim p_{\text{train}}$, $\epsilon \sim p_{\text{noise}}(\cdot; \sigma)$.

Instead of using the log-normal distribution for p_{train} that is suggested in [Karras et al. \(2022\)](#), we construct a distribution whose quantiles match the noise-level schedule used for sample generation, assigning higher probability to noise levels which are closer together during sampling. Details are in Appendix A.3.2. As in [Lam et al. \(2023\)](#) we weight the squared error made at each latitude-longitude grid cell by a per-variable-level loss weight, as well as the normalized area of that grid cell; this is also a departure from [Karras et al. \(2022\)](#).

The optimisation hyperparameters used for training are summarised in Appendix A.5. It is worth noting that unlike GraphCast, which is fine-tuned by back-propagating gradients through 12 step trajectories (3 days with 6h steps) produced by feeding the model its own inputs during training, GenCast is only ever trained using data from a single 12h transition between a current and future state, without ever seeing its own predictions as inputs during training. Nonetheless, GenCast is still able to roll out for 15 days and produce better results than GraphCast.

3.3. Training data

We trained GenCast on a dataset built from the ECMWF’s ERA5 archive ([Hersbach et al., 2020](#)), a large corpus of global reanalysis data. Our ERA5 dataset contains a subset of the variables from the ERA5 archives on 13 pressure levels (see Table A.1 for complete list of variables and pressure levels), on a 1° equiangular grid. To generate the 1° dataset, we downloaded data on a 0.25° equiangular grid from the ERA5 archive, then subsampled it to 1° with simple 1-in-4 subsampling. We also subsampled the temporal resolution from 1 hour to 6 hours, corresponding to 00z, 06z, 12z and 18z times each day, where 00z means 00:00 UTC in Zulu convention. From this dataset, we extracted sequences at 12 hour temporal resolution (sequences of 00z/12z or 06z/18z times) to train GenCast.

Although its temporal resolution is hourly, ERA5 only assimilates observations in 12-hour windows, from 21z-09z and 09z-21z. This means that steps taken within a single 12h assimilation window have a different, less dispersed distribution to those which jump from one window into the next. By choosing a 12 hour time step we avoid training on this bimodal distribution, and ensure that our model always predicts a target from the next assimilation window.

For accumulated variables such as precipitation, instead of subsampling the data in time, we accumulated values over the 12 hour period preceding each time.

Our dataset covers the period of 1979 to 2019. During the development phase of GenCast, we used dates from 1979 to 2017 for training and validated results on 2018. Before starting the test phase, we froze all model and training choices, retrained the model on data from 1979 to 2018, and evaluated results on 2019. For the perturbed ensemble baseline, we trained the deterministic GraphCast baseline with the protocol described in [Lam et al. \(2023\)](#) at 0.25° resolution, using data from 1979 to 2018, which is consistent with the approach to the data split for GenCast.

4. Verification

4.1. Baseline models

4.1.1. ENS

We compare GenCast to ECMWF’s operational ensemble forecast, ENS. ENS is generated using ECMWF’s Integrated Forecast System (IFS), a state-of-the-art numerical weather prediction system ([ECMWF, 2019](#)). It consists of 50 perturbed ensemble members, and one unperturbed control member which we exclude from our evaluation. During our 2019 test period, ENS ran at 0.16° horizontal resolution, half that of ECMWF’s high-resolution (HRES) deterministic forecast.³ It was initialized using the HRES deterministic analysis, perturbed using ECMWF’s operational ensemble of data assimilations (EDA) together with additional flow-dependent singular value perturbations. This initialization strategy was first proposed by [Buizza et al. \(2008\)](#), who found the singular value perturbations were necessary because EDA perturbations alone give an under-dispersed ensemble. ENS also applies stochastic perturbations to parameterisation tendencies (SPPT) at each solver step during model integration ([Buizza et al., 1999](#)). We downloaded ENS forecasts from the TIGGE ([Bougeault et al., 2010](#)) archive, an initiative of the World Weather Research Programme (WWRP), and regridded them to 0.25° . We then performed 1-in-4 subsampling of both forecasts and targets from 0.25° to 1° for evaluation. This avoids smoothing out high-frequency components of error, and matches the subsampling we applied to ERA5 when training and evaluating GenCast. We chose this subsampling approach, such that models that run at a coarser resolution that is a multiple of 0.25° (e.g. GenCast running at 1°) can still be evaluated on the same statistics of metrics produced by detailed higher resolution 0.25° forecasts (e.g. GraphCast or ENS).

The public TIGGE archive makes all 50 ENS ensemble members available at 8 of the 13 pressure levels forecasted by GenCast. We thus perform all primary evaluation and comparisons using 50-member ensembles for all models.

4.1.2. Perturbed GraphCast ensemble

As an ML baseline we use GraphCast ([Lam et al., 2023](#)) to generate ensemble forecasts (denoted GraphCast-Perturbed). Since GraphCast is a deterministic model, all ensemble spread must come from

³As of June 2023, ENS has been upgraded to match the resolution of HRES.

differences in the initial conditions. We initialize GraphCast using the deterministic ERA5 analysis plus two additional perturbations:

- ERA5 EDA perturbations, analogous to the operational EDA perturbations used to initialize ENS. These are computed as $\Delta_i^{EDA} = e_i - \bar{e}$, where e_i are the 9 perturbed members of the ERA5 EDA, and \bar{e} is their mean.
- Ad-hoc Gaussian Process perturbations Δ_i^{GP} . These are sampled from a Gaussian Process on the sphere with a horizontal decorrelation length-scale of 1200km and marginal standard deviations of 0.085 times those of 6-hour differences in each perturbed variable and level. These perturbations improve skill at longer lead times over EDA perturbations alone, and allow us to increase the ensemble size beyond that of the EDA ensemble; full details are in Appendix A.4.

4.2. Ensemble initial conditions for GenCast

We initialize GenCast using deterministic ERA5 analysis plus the ERA5 EDA perturbations Δ_i^{EDA} described above. Unlike for GraphCast-Perturbed, we do not include additional Gaussian Process perturbations as we did not find them to improve skill.

4.3. Verification protocol

For a fair comparison of both models at short lead times, we evaluate each model against its own analysis. Specifically we follow the protocol described in Lam et al. (2023, Appendix Section 5.2) in which we evaluate ECMWF’s operational forecasts against HRES-fc0 (a dataset comprising the initial conditions used for their HRES deterministic forecast), and we evaluate ML models trained and initialized using ERA5, against ERA5.

During our 2019 test period, ENS was initialized using analyses making use of between 3 and 5 hours of assimilation window look-ahead beyond the stated initialization time (Lean et al., 2019). Again following the protocol established in Lam et al. (2023), we initialize ML models using the 06z and 18z values of ERA5, since these benefit from only 3 hours of look-ahead, as compared to the 9 hours of look-ahead from which the 00z and 12z values benefit⁴. In Figure A.11 we show that the impact of the assimilation window look-ahead in the initial conditions is indeed substantial. Evaluating GenCast’s forecasts initialized with 00z/12z (as compared with 06z/18z) values yields substantial and consistent improvements in both CRPS and Ensemble-Mean RMSE, confirming that accounting for this look-ahead is important for fair comparisons between models. Overall the difference in assimilation windows used in our evaluation leaves ENS with a small advantage of up to 2 hours additional look-ahead over the ML models, for all variables except SST.

Ideally we would compare all models at the same 06z/18z initialization times, however ENS forecasts from 06z/18z are only archived up to 6 day lead times. Furthermore, we have not been able to complete the download of these 06z/18z forecasts, and so we compare ENS at 00z/12z with the ML models at 06z/18z. Lam et al. (2023) found that 00z/12z initialization tends to give a small advantage to the deterministic HRES forecast over the 06z/18z initialization, and we expect a similar minor advantage to apply to ENS.

We follow standard verification practice (W.M.O., 2019, Section 2.2.35) in evaluating ensemble forecasts using a single deterministic analysis as ground truth. However we note that this rewards

⁴An exception is sea surface temperature (SST), which in ERA5 is updated once per 24 hours based on a longer assimilation window; however this is a relatively slow-changing variable and we don’t believe any extra look-ahead in this particular case to have a material effect.

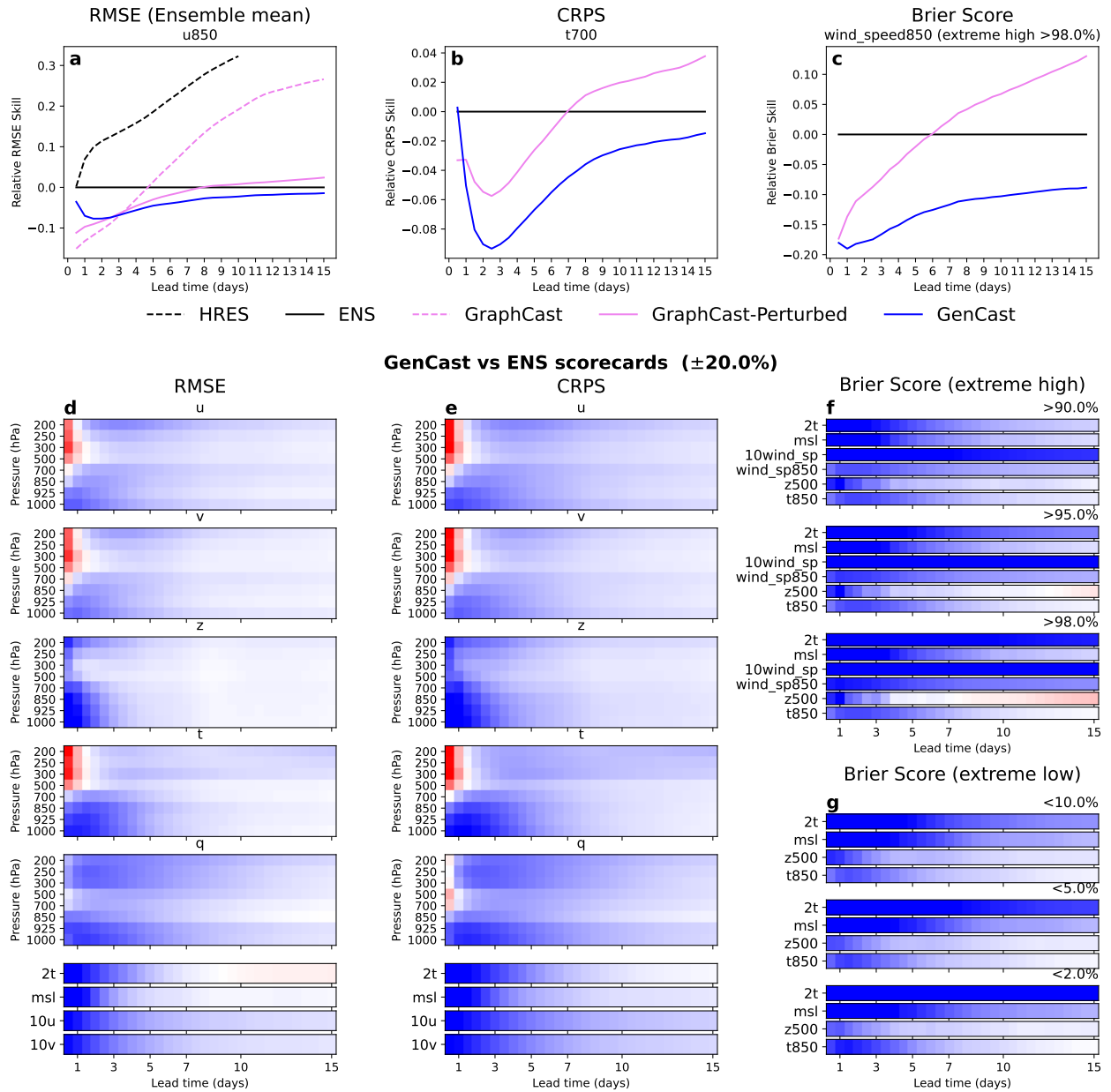


Figure 2 | Predictive skill of GenCast compared to ENS and GraphCast-Perturbed, evaluated using probabilistic metrics over ensembles of trajectories. (a) Ensemble-Mean RMSE Skill of longitudinal wind at 850hPa, relative to ENS (lower is better). (b) CRPS Skill of temperature at 700hPa (lower is better), relative to ENS. (c) Brier score for top 2% events in wind magnitude at 850 hPa (lower is better), relative to ENS. (d) Scorecard comparing Ensemble-Mean RMSE skill between GenCast and ENS across all variables and 8 pressure levels, where dark blue (resp. red) means GenCast is 30% better (resp. worse) than ENS, and white means the perform equally. (e) Similar scorecard comparing CRPS. (f-g) Similar scorecard comparing Brier score for (f) extreme high and (g) extreme low events. The variables and levels shown in panels a, b, and c were chosen on the basis of being generally representative both of the overall relative performance (all three are at or below median performance for that metric when averaged over lead time), and in terms of qualitative characteristics of the curves. The results indicate that GenCast performs better than ENS on more than 96% of all reported variable-leadtime-level combinations on all three metrics.

under-dispersion at short lead times—for example at lead time zero, scores computed against deterministic analysis would be optimized by setting all initial conditions equal to the deterministic analysis, ignoring initial condition uncertainty. In future work we believe that scoring ensemble forecasts against ensemble analysis (as proposed for example by Radanovics et al. (2018)) would be informative, especially in relation to skill and reliability at short lead times.

5. Results

5.1. Predictive skill

We assess the predictive skill of GenCast via comparison of the Continuous Ranked Probability Score (CRPS, Appendix A.6.1) and the RMSE of the ensemble mean (Appendix A.6.3), across all variables and pressure levels. Figure 2 shows scorecards comparing the CRPS achieved by GenCast compared to that achieved by ENS. Blue on the scorecard indicates superior (i.e. lower) CRPS for GenCast, while red indicates that ENS performed better. GenCast outperforms ENS in 97.3% of cases⁵, and 100% of cases at a lead time of more than 36h. The mean improvement in CRPS across all lead times is 4.8% for atmospheric variables and 7.9% for surface variables, with the gap between GenCast and ENS shrinking as lead time increases towards 15 days.

A similar set of scorecards comparing the Ensemble-Mean RMSE are also shown in Figure 2. The relative performance of GenCast compared to ENS is similar on Ensemble-Mean RMSE to what is observed for CRPS. GenCast outperforms ENS in 96.4% of cases, and 98.7% of cases at a lead time of more than 36h (the only exception being 2m temperature from 9 days to 15 day, where ENS is marginally better, by up to 1.3%). The mean improvement in Ensemble-Mean RMSE across all lead times is 3.5% for atmospheric variables and 5.4% for surface variables, and once again the gap tends to peak within the first 3 days, and decrease as lead time increases.

In Figure A.10, we show the CRPS and RMSE scorecards comparing GenCast to GraphCast-Perturbed, which confirm the substantial improvement yielded by GenCast.

5.2. Predicting extremes

One important motivation for ensemble forecasts, and probabilistic forecasting generally, is the ability to predict the probability of rare events. We assess performance of the three models on extreme-event prediction by calculating Brier scores (Appendix A.6.2) for the exceedance of high and low percentiles of the climatological distribution (climatological percentiles are computed for each variable on a per-latitude, longitude, month-of-year and time-of-day basis, using 24 years of ERA5 from 1993 to 2016). Figure 2 shows a relative performance scorecard of GenCast compared to ENS on Brier scores for <2nd, <5th, <10th, >90th, >95th, and >98th percentile events, for msl, z500, 2t, t850, 10m wind speed, and wind speed at 850hPa across all lead times. GenCast outperforms ENS in 97.6% of these 900 cases, with an average relative improvement of 12.6%.

5.3. Physical plausibility

5.3.1. Spherical harmonic power spectra

An important strength of GenCast is its ability to generate physically plausible ensemble members (see Figure 3). In contrast, a notable characteristic of RMSE-trained ML forecasting models like GraphCast

⁵Note that we exclude results on precipitation from our main results, and defer them to Appendix A.7.1, with the caveat that we lack full confidence in the quality of ERA5 precipitation data, and that we have not tailored our evaluation to precipitation specifically beyond adding SEEPS as a further metric.

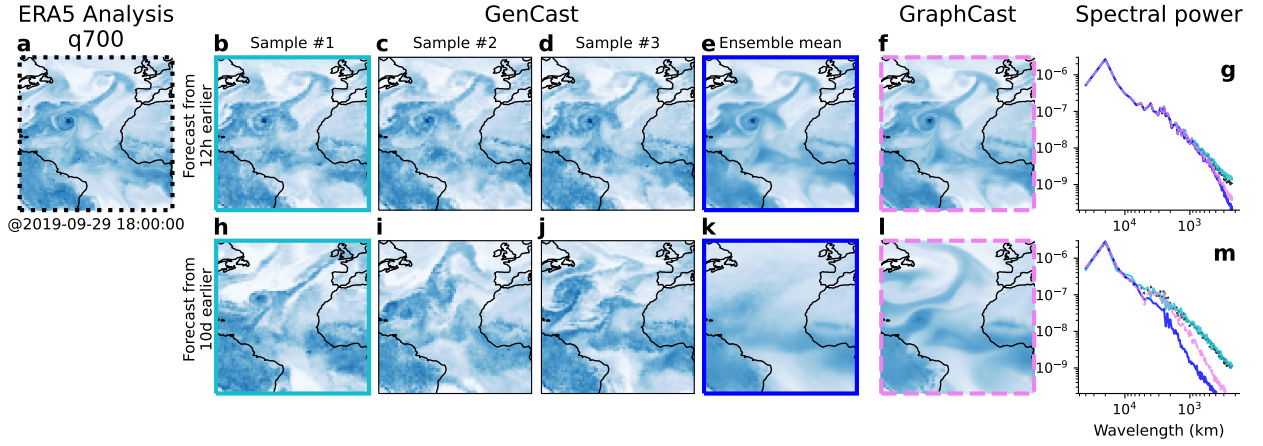


Figure 3 | Visualization of representative states produced by GenCast compared to GraphCast. (a) ERA5 analysis state for specific humidity at 700hPa at 6pm on the 29th of September of 2019. (b-d) 3 sample forecasts of this state by GenCast from 12 hours earlier. (e) Ensemble average obtained by taking the mean of 50 sample forecasts by GenCast from 12 hours earlier. (f) Forecast by the GraphCast (model which is deterministic), made 12 hours earlier. (g) Spectrum of the fields shown in panels (a-f), with colors matching the frames of the panels. (h-m) Same as (b-g), but for forecasts made 10 days earlier. Unlike deterministic GraphCast, which expresses uncertainty as blurring which increases with lead time (f, l), we observe how the sample forecasts produced by GenCast are sharp (g, m), regardless of whether the forecasts are for 12 hours ahead (g, b-d) (where the three samples are very similar) or 10 days ahead (m, h-j) (where the three samples differ more). The samples can still be averaged to produced a blurry mean state (e, k). Additional visualizations and an explanation of how this date/time was selected for visualisation are available in Appendix A.8.

is that they model something closer to the mean trajectory, rather than individual realizations, and as a result tend to generate blurred (and therefore physically implausible) forecasts for longer lead times. When RMSE-trained models are used to generate ensembles by rolling out from perturbed initial conditions, the ensemble members inherit this shortfall, resulting in an ensemble of ‘unphysical’ predictions, all of which lack sharp detail.

One proxy for assessing the physical plausibility of the forecasts is to examine the extent to which their spherical harmonic power spectra match those found in the ground truth/targets. Figure 4 compares the mean spherical harmonic power spectra of forecasts generated by GenCast and GraphCast-Perturbed to the those of the ground-truth targets, for different variables at different lead times. As expected, GraphCast-Perturbed has significantly less power at high frequencies at longer lead times than the ground truth, which corresponds to the blurring noted above. In contrast, GenCast’s predictions have a power spectrum which preserves high frequency content and much more closely matches that of the ground truth.

For smoother variables with many orders of magnitude less power at high frequencies than low frequencies, like z500, we note that GenCast’s forecasts can contain some additional high-frequency content at longer lead times which is not present in the ground truth, as shown in Figure 4f. However, the magnitude of these deviations is very small (at least 6 orders of magnitude smaller than the dominant powers in the case of z500) and the range of affected wavelengths is small, such that this does not meaningfully affect the forecast signal. Power spectra plots for additional variables and lead-times are included in Figure A.8 and Figure A.9.

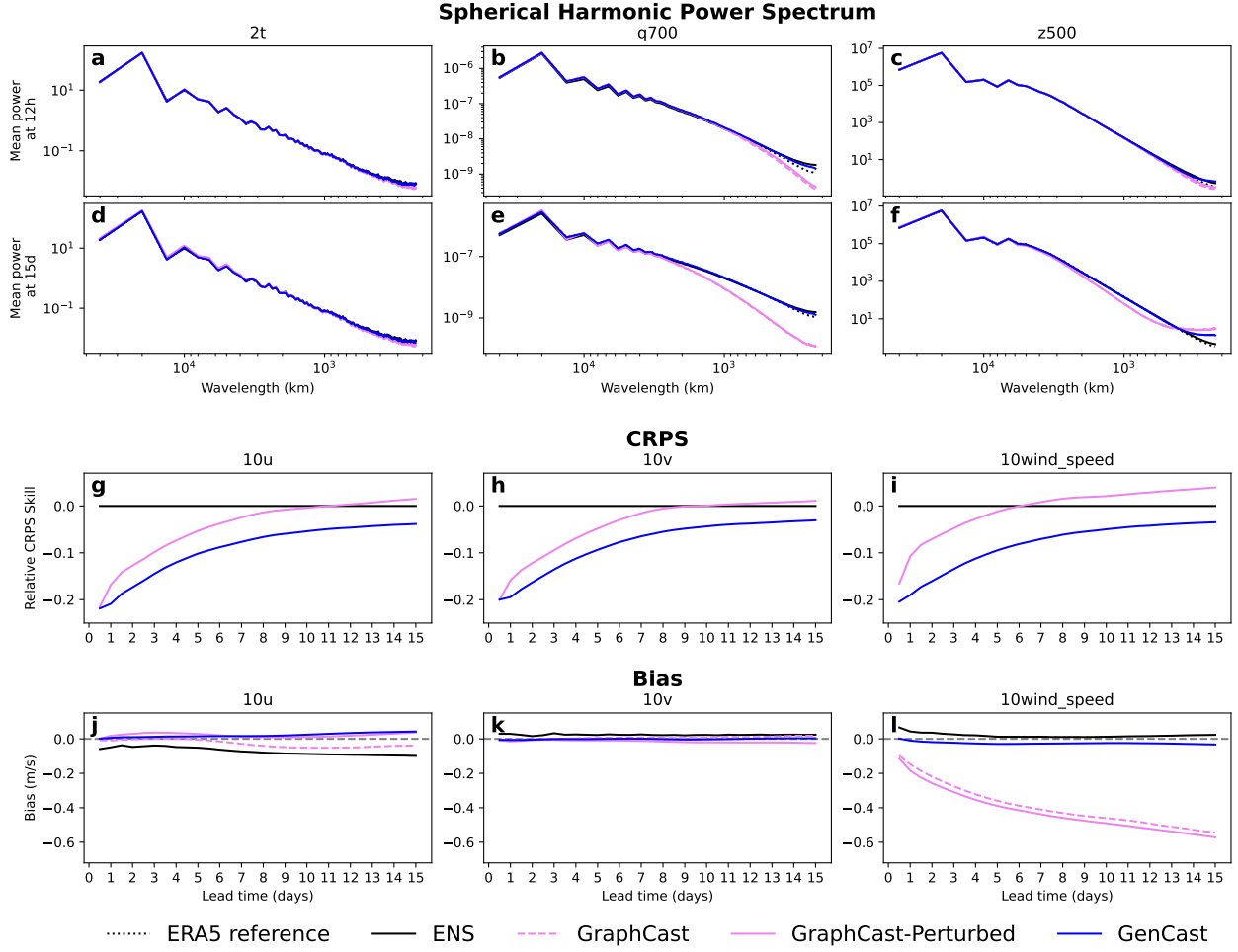


Figure 4 | Comparing physical plausibility of the states produced by GenCast, ENS, and GraphCast-Perturbed using spectral metrics and derived variables. (a-f) Spherical harmonic power spectrum comparison between the three models as function of the lead-time for 2t, q700, and z500. Similar to ENS (black), the states produced by GenCast (blue) show spectral properties that are close to that of analysis states (dotted line). The only exception are very smooth variables, where our GenCast produces a very small amount of high frequency noise (6 or 7 orders of magnitude smaller than the dominant powers). On the other hand GraphCast-Perturbed, struggles to preserve high frequency components, especially at long lead-times. (g-l) Comparison of the (g-i) relative CRPS (lower is better) and (j-l) bias (close to zero is better) performance on native surface wind components 10u and 10v (g-h, j-k), and derived wind speed (i, l). We observed how the performance of GraphCast-Perturbed is relatively stronger on the variables that it was trained to predict (wind components), than it is on the derived variable (wind speed), exhibiting poorer relative CRPS and a strong negative bias for wind magnitude. On the other hand GenCast performs similarly well on both the wind components (which was trained to the predict), and the wind speed (which is derived). This seems to support the hypothesis that the states produced by GenCast are more physically plausible than GraphCast-Perturbed, similar to the states produced by ENS.

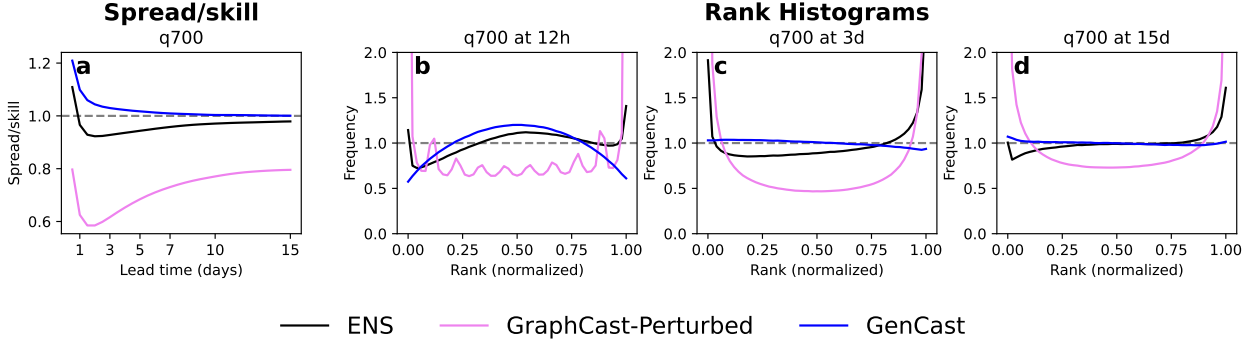


Figure 5 | Evaluation of the reliability and spread of the ensembles produced by GenCast, ENS, and GraphCast-Perturbed. (a) Spread/skill ratio for specific humidity at 700hPa (closer to 1 is better, higher suggests over-dispersion and lower under-dispersion) as function of lead time. (b-d) Rank histograms for specific humidity at 700hPa (flatter is better, U-shape suggests under-dispersion and \cap -shape over-dispersion) at (b) 12 hours, (c) 3 days, and (d) 15 days lead time. We observed that while GenCast appears over dispersed in short lead times (similarly to ENS), it is otherwise well-calibrated. On the other hand ENS can display some under-dispersion at intermediate lead times, and GraphCast-Perturbed is generally under-dispersed for all lead times.

5.3.2. Predicting non-linear derived variables

GenCast also improves upon a further shortcoming of models like GraphCast and GraphCast-Perturbed which are trained to minimize RMSE, specifically their tendency to produce biased and less accurate forecasts of non-linear derived quantities, such as wind speed (i.e., the L2-norm of the (u,v) wind vector: $\sqrt{u^2 + v^2}$). Fundamentally this arises because a non-linear function of an expectation is not equal to the expectation of the function. Figure 4 compares GenCast with GraphCast-Perturbed (and ENS) on both CRPS and forecast bias for 10u, 10v, and 10wind_speed, where the wind speed variable is calculated as a function of the u and v forecasts. The most striking feature of GraphCast-Perturbed in Figure 4 is that while it exhibits minimal bias on 10u and 10v— indeed, less than ENS—it exhibits a significant negative bias in its derived wind speed forecasts, in particular at longer lead-times. GenCast, on the other hand, exhibits minimal bias on the derived 10wind_speed, in addition to the very small bias it displays for 10u, 10v. Moreover, as shown in the top row of plots in Figure 4, while on CRPS the relative performance of GraphCast-Perturbed against ENS is worse for 10wind_speed than for 10u and 10v, GenCast maintains the advantage it has over ENS for 10wind_speed as well.

5.4. Reliability and spread

Two common methods for evaluating the reliability of ensemble forecasts are the spread-skill relationship (Fortin et al., 2014; Leutbecher, 2009) and rank histograms (Talagrand, 1999). Figure 5 displays a spread/skill ratio (defined in Appendix A.6.4) as a function of lead time, together with rank histograms at 12 hours, 3 days, and 15 days, for GenCast, GraphCast-Perturbed, and ENS on q700.

For perfect ensemble forecasts in which ensemble members and ground truth are all exchangeable, we expect on average to see a flat rank histogram, and a spread/skill ratio of 1. While diagnosis of under- or over-dispersion is confounded by forecast bias (Hamill, 2001; Wilks, 2011), if we assume such bias is relatively small, we can associate under-dispersion on average approximately with spread/skill < 1 and a U-shaped rank histogram; and over-dispersion on average with spread/skill > 1 and a \cap -shaped rank histogram.

As shown in Figure 5, generally GenCast’s spread/skill and rank histograms tend to be as good, or better, than ENS’s, and much better than GraphCast-Perturbed’s.

The spread-skill plot in Figure 5a shows GenCast converging to a spread-skill score close to 1 within 3-4 days. In contrast, spread/skill for ENS is consistent with slight under-dispersion from 1-2 days onward, and GraphCast-Perturbed with substantial under-dispersion throughout. These results are typical of what is observed for other variables too, see Figure A.5.

At 12h (Figure 5b), the rank histograms are consistent with both GenCast and ENS being over-dispersed. However we caution that we are evaluating forecasts initialized from ensemble analysis against a deterministic analysis. While this is standard practise, as noted in Section 4.3 this unduly rewards under-dispersion at short lead times and may make a correctly-dispersed forecast at short lead time look over-dispersed. GraphCast-Perturbed shows under-dispersed forecasts in two ways. At a high level, it shows a U-shaped rank histogram. But also, the overall shape is modulated by 10 characteristic peaks, which indicates that at the 12h lead time, the variance between forecasts is mostly dominated by the 9 members of the EDA perturbations, but not so much by the additional ad-hoc Gaussian process perturbations.

In the 3d and 15d rank histograms (Figure 5c and d, respectively), however, GenCast exhibits very flat rank histograms. ENS tends to consistently display some under-dispersion at 3d, while its rank histograms at 15d tend to be flat, though with some examples of a slight under-prediction bias. GraphCast-Perturbed generally appears under-dispersed at all lead times, however, increasing the scale of the Gaussian process perturbations beyond 0.085 negatively impacts CRPS metrics, see Appendix A.4.4 for detail. These results are typical of the results observed for other variables too, as shown by the additional rank histogram plots in Figure A.6 and Figure A.7.

6. Conclusions

We have presented GenCast, a new approach for global medium range ensemble weather forecasting up to 15 days into the future, using a diffusion model to sample ensembles from the joint distribution over future weather trajectories. Evaluation on three key skill metrics (Ensemble-Mean RMSE, CRPS, and Brier scores) shows that GenCast consistently outperforms ECMWF’s ENS system on 15-day global weather forecasts, at 1° latitude-longitude resolution, at all 8 (out of 13) pressure levels we were able to evaluate, as well as on surface variables. Our evaluation of the power spectral density of GenCast’s predicted states and the quality of derived-variable forecasts shows that high-frequency spatial structure and physical consistency is well-preserved throughout the forecast trajectories. Analysis of spread/skill ratios and rank histograms shows that GenCast’s ensembles are as-or-more reliable than those of ENS. Producing a single 15-day trajectory with GenCast takes around a minute on a Cloud TPU v4, and so N ensemble members can also be generated in around a minute with N TPUs, enabling the use of orders of magnitude larger ensembles in the future.

While GenCast has key advantages over traditional approaches, there is also room for further advances. GenCast operates at 1° resolution while ENS operated at 0.16° until mid-2023, and now operates at 0.081° . Moreover, as a diffusion model, GenCast is computationally more expensive than an equivalent architecture deployed as a standard deterministic ML forecasting model, due to the multiple function evaluations required to sample each forecast timestep. Thus we chose 1° here to make training and inference faster. For operational use, GenCast should be trained and tested at higher resolution, and would likely yield better results. GenCast also relies on initial conditions from a traditional NWP ensemble data assimilation system, and therefore for operational use those systems must still be available.

Broadly, though, GenCast represents an important step forward for ML-based weather forecasting, by providing greater skill than the top operational ensemble forecast, at 1° resolution. This work helps open the door to a new era of ensemble forecasting based on ML, broadening its applicability and utility to a wider range of domains.

7. Acknowledgments

Andrew El-Kadi contributed to this work during an internship at Google DeepMind. In alphabetical order, we thank Alexis Boukouvalas, Matthew Chantry, Yuri Chervonyi, Sander Dieleman, Praneet Dutta, Marta Garnelo, Xavier Glorot, Stephan Hoyer, Amy Li, Rahul Mahrsee, Piotr Mirowski, Kevin Murphy, Charlie Nash, Nick Pezzotti, Stephan Rasp, Suman Ravuri, Daniel Rothenberg, Tim Salimans, Fei Sha, Kunal Shah, Octavian Voicu, David Wallis, Daniel Worrall, and Flora Xue.

References

- M. Andrychowicz, L. Espeholt, D. Li, S. Merchant, A. Merose, F. Zyda, S. Agrawal, and N. Kalchbrenner. Deep learning for day forecasts from sparse observations. *arXiv preprint arXiv:2306.06079*, 2023.
- A. Asperti, F. Merizzi, A. Paparella, G. Pedrazzi, M. Angelinelli, and S. Colamonaco. Precipitation nowcasting with generative diffusion models. *arXiv preprint arXiv:2308.06733*, 2023.
- G. Batzolis, J. Stanczuk, C.-B. Schönlieb, and C. Etmann. Conditional image generation with score-based diffusion models. *arXiv preprint arXiv:2111.13606*, 2021.
- K. Bi, L. Xie, H. Zhang, X. Chen, X. Gu, and Q. Tian. Pangu-Weather: A 3D high-resolution model for fast and accurate global weather forecast. *arXiv preprint arXiv:2211.02556*, 2022.
- K. Bi, L. Xie, H. Zhang, X. Chen, X. Gu, and Q. Tian. Accurate medium-range global weather forecasting with 3d neural networks. *Nature*, 619(7970):533–538, 2023.
- A. Blattmann, R. Rombach, H. Ling, T. Dockhorn, S. W. Kim, S. Fidler, and K. Kreis. Align your latents: High-resolution video synthesis with latent diffusion models. In *Proceedings of the IEEE/CVF Conference on Computer Vision and Pattern Recognition*, pages 22563–22575, 2023.
- P. Bougeault, Z. Toth, C. Bishop, B. Brown, D. Burridge, D. H. Chen, B. Ebert, M. Fuentes, T. M. Hamill, K. Mylne, J. Nicolau, T. Paccagnella, Y.-Y. Park, D. Parsons, B. Raoult, D. Schuster, P. S. Dias, R. Swinbank, Y. Takeuchi, W. Tennant, L. Wilson, and S. Worley. The thorpe interactive grand global ensemble. *Bulletin of the American Meteorological Society*, 91(8):1059 – 1072, 2010. doi: <https://doi.org/10.1175/2010BAMS2853.1>. URL https://journals.ametsoc.org/view/journals/bams/91/8/2010bams2853_1.xml.
- R. Buizza, M. Milleer, and T. N. Palmer. Stochastic representation of model uncertainties in the ECMWF ensemble prediction system. *Quarterly Journal of the Royal Meteorological Society*, 125(560):2887–2908, 1999.
- R. Buizza, M. Leutbecher, and L. Isaksen. Potential use of an ensemble of analyses in the ECMWF ensemble prediction system. *Quarterly Journal of the Royal Meteorological Society*, 134(637): 2051–2066, 2008.
- K. Chen, T. Han, J. Gong, L. Bai, F. Ling, J.-J. Luo, X. Chen, L. Ma, T. Zhang, R. Su, et al. Fengwu: Pushing the skillful global medium-range weather forecast beyond 10 days lead. *arXiv preprint arXiv:2304.02948*, 2023.

- M. Chen, X. Tan, B. Li, Y. Liu, T. Qin, S. Zhao, and T.-Y. Liu. Adaspeech: Adaptive text to speech for custom voice, 2021.
- J. R. Driscoll and D. M. Healy. Computing fourier transforms and convolutions on the 2-sphere. *Adv. Appl. Math.*, 15(2):202–250, June 1994.
- ECMWF. *IFS Documentation CY46R1 - Part V: Ensemble Prediction System*. 2019. doi: 10.21957/38yug0cev. URL <https://www.ecmwf.int/node/19309>.
- L. Edward. The essence of chaos. 1993.
- V. Fortin, M. Abaza, F. Anctil, and R. Turcotte. Why should ensemble spread match the rmse of the ensemble mean? *Journal of Hydrometeorology*, 15(4):1708–1713, 2014.
- Z. Gao, X. Shi, B. Han, H. Wang, X. Jin, D. Maddix, Y. Zhu, M. Li, and Y. Wang. Prediff: Precipitation nowcasting with latent diffusion models. *arXiv preprint arXiv:2307.10422*, 2023.
- T. Gneiting and A. E. Raftery. Strictly proper scoring rules, prediction, and estimation. *Journal of the American statistical Association*, pages 359–378, 2007.
- T. Haiden, M. J. Rodwell, D. S. Richardson, A. Okagaki, T. Robinson, and T. Hewson. Intercomparison of global model precipitation forecast skill in 2010/11 using the seeps score. *Monthly Weather Review*, 140(8):2720–2733, 2012.
- T. M. Hamill. Interpretation of rank histograms for verifying ensemble forecasts. *Monthly Weather Review*, 129(3):550–560, 2001.
- W. Harvey, S. Naderiparizi, V. Masrani, C. Weilbach, and F. Wood. Flexible diffusion modeling of long videos. *Advances in Neural Information Processing Systems*, 35:27953–27965, 2022.
- H. Hersbach, B. Bell, P. Berrisford, S. Hirahara, A. Horányi, J. Muñoz-Sabater, J. Nicolas, C. Peubey, R. Radu, D. Schepers, et al. The ERA5 global reanalysis. *Quarterly Journal of the Royal Meteorological Society*, 146(730):1999–2049, 2020.
- J. Ho, A. Jain, and P. Abbeel. Denoising diffusion probabilistic models. *Advances in neural information processing systems*, 33:6840–6851, 2020.
- J. Ho, W. Chan, C. Saharia, J. Whang, R. Gao, A. Gritsenko, D. P. Kingma, B. Poole, M. Norouzi, D. J. Fleet, et al. Imagen video: High definition video generation with diffusion models. *arXiv preprint arXiv:2210.02303*, 2022a.
- J. Ho, T. Salimans, A. Gritsenko, W. Chan, M. Norouzi, and D. J. Fleet. Video diffusion models, 2022b.
- J. Hu, X. Liu, Z. Fan, Y. Liang, and R. Zimmermann. Towards unifying diffusion models for probabilistic spatio-temporal graph learning, 2023.
- N. Jouppi, G. Kurian, S. Li, P. Ma, R. Nagarajan, L. Nai, N. Patil, S. Subramanian, A. Swing, B. Towles, et al. Tpu v4: An optically reconfigurable supercomputer for machine learning with hardware support for embeddings. In *Proceedings of the 50th Annual International Symposium on Computer Architecture*, pages 1–14, 2023.
- E. Kalnay. *Atmospheric modeling, data assimilation and predictability*. Cambridge university press, 2003.
- T. Karras, M. Aittala, T. Aila, and S. Laine. Elucidating the design space of diffusion-based generative models. *Advances in Neural Information Processing Systems*, 35:26565–26577, 2022.

- R. Keisler. Forecasting global weather with graph neural networks. *arXiv preprint arXiv:2202.07575*, 2022.
- D. Kochkov, J. Yuval, I. Langmore, P. Norgaard, J. Smith, G. Mooers, J. Lottes, S. Rasp, P. Düben, M. Klöwer, et al. Neural general circulation models. *arXiv preprint arXiv:2311.07222*, 2023.
- G. Kohl, L.-W. Chen, and N. Thuerey. Turbulent flow simulation using autoregressive conditional diffusion models. *arXiv preprint arXiv:2309.01745*, 2023.
- T. Kurth, S. Subramanian, P. Harrington, J. Pathak, M. Mardani, D. Hall, A. Miele, K. Kashinath, and A. Anandkumar. FourCastNet: Accelerating global high-resolution weather forecasting using adaptive fourier neural operators. *arXiv preprint arXiv:2208.05419*, 2022.
- R. Lam, A. Sanchez-Gonzalez, M. Willson, P. Wirnsberger, M. Fortunato, A. Pritzel, S. Ravuri, T. Ewalds, F. Alet, Z. Eaton-Rosen, et al. Graphcast: Learning skillful medium-range global weather forecasting. *arXiv preprint arXiv:2212.12794*, 2022.
- R. Lam, A. Sanchez-Gonzalez, M. Willson, P. Wirnsberger, M. Fortunato, F. Alet, S. Ravuri, T. Ewalds, Z. Eaton-Rosen, W. Hu, et al. Learning skillful medium-range global weather forecasting. *Science*, page eadi2336, 2023.
- P. Lean, M. Bonavita, E. Hólm, N. Bormann, and T. McNally. Continuous data assimilation for the IFS. *ECMWF Newsletter*, pages 21–26, Jan. 2019. doi: 10.21957/9pl5fc37it. URL <https://www.ecmwf.int/node/18882>.
- M. Leutbecher. Diagnosis of ensemble forecasting systems. In *Seminar on diagnosis of forecasting and data assimilation systems*, pages 235–266, 2009.
- H. Li, L. Chen, X. Zhong, F. Zhang, Y. Cheng, Y. Xu, and Y. Qi. Fuxi: A cascade machine learning forecasting system for 15-day global weather forecast. *npj Climate and Atmospheric Science*, 6(190), 2023a.
- L. Li, R. Carver, I. Lopez-Gomez, F. Sha, and J. Anderson. Seeds: Emulation of weather forecast ensembles with diffusion models. *arXiv preprint arXiv:2306.14066*, 2023b.
- I. Loshchilov and F. Hutter. Decoupled weight decay regularization. In *International Conference on Learning Representations*, 2018.
- C. Lu, Y. Zhou, F. Bao, J. Chen, C. Li, and J. Zhu. DPM-Solver++: Fast solver for guided sampling of diffusion probabilistic models. *arXiv preprint arXiv:2211.01095*, 2022.
- T. Nguyen, R. Shah, H. Bansal, T. Arcomano, S. Madireddy, R. Maulik, V. Kotamarthi, I. Foster, and A. Grover. Scaling transformer neural networks for skillful and reliable medium-range weather forecasting. *arXiv preprint arXiv:2312.03876*, 2023.
- T. Q. Nguyen and J. Salazar. Transformers without tears: Improving the normalization of self-attention. In *Proceedings of the 16th International Conference on Spoken Language Translation*, 2019.
- R. North, M. Trueman, M. Mittermaier, and M. J. Rodwell. An assessment of the seeps and sedi metrics for the verification of 6 h forecast precipitation accumulations. *Meteorological Applications*, 20(2):164–175, 2013.
- T. Palmer. The ecmwf ensemble prediction system: Looking back (more than) 25 years and projecting forward 25 years. *Quarterly Journal of the Royal Meteorological Society*, 145:12–24, 2019.

- T. Palmer and R. Hagedorn. *Predictability of weather and climate*. Cambridge University Press, 2006.
- J. Pathak, S. Subramanian, P. Harrington, S. Raja, A. Chattopadhyay, M. Mardani, T. Kurth, D. Hall, Z. Li, K. Azizzadenesheli, et al. Fourcastnet: A global data-driven high-resolution weather model using adaptive fourier neural operators. *arXiv preprint arXiv:2202.11214*, 2022.
- S. Radanovics, J.-P. Vidal, and E. Sauquet. Spatial verification of ensemble precipitation: An ensemble version of SAL. *Weather Forecast.*, 33(4):1001–1020, Aug. 2018.
- S. Rasp, P. D. Dueben, S. Scher, J. A. Weyn, S. Mouatadid, and N. Thuerey. WeatherBench: a benchmark data set for data-driven weather forecasting. *Journal of Advances in Modeling Earth Systems*, 12(11):e2020MS002203, 2020.
- S. Rasp, S. Hoyer, A. Merose, I. Langmore, P. Battaglia, T. Russel, A. Sanchez-Gonzalez, V. Yang, R. Carver, S. Agrawal, et al. Weatherbench 2: A benchmark for the next generation of data-driven global weather models. *arXiv preprint arXiv:2308.15560*, 2023.
- K. Rasul, C. Seward, I. Schuster, and R. Vollgraf. Autoregressive denoising diffusion models for multivariate probabilistic time series forecasting. In *International Conference on Machine Learning*, pages 8857–8868. PMLR, 2021.
- S. Ravuri, K. Lenc, M. Willson, D. Kangin, R. Lam, P. Mirowski, M. Fitzsimons, M. Athanassiadou, S. Kashem, S. Madge, et al. Skilful precipitation nowcasting using deep generative models of radar. *Nature*, 597(7878):672–677, 2021.
- N. Roberts, B. Ayliffe, G. Evans, S. Moseley, F. Rust, C. Sandford, T. Trzeciak, P. Abernethy, L. Beard, N. Crosswaite, et al. Improver: The new probabilistic postprocessing system at the met office. *Bulletin of the American Meteorological Society*, 104(3):E680–E697, 2023.
- M. J. Rodwell, D. S. Richardson, T. D. Hewson, and T. Haiden. A new equitable score suitable for verifying precipitation in numerical weather prediction. *Quarterly Journal of the Royal Meteorological Society*, 136(650):1344–1363, 2010.
- J. Sohl-Dickstein, E. Weiss, N. Maheswaranathan, and S. Ganguli. Deep unsupervised learning using nonequilibrium thermodynamics. In *International conference on machine learning*, pages 2256–2265. PMLR, 2015.
- Y. Song, J. Sohl-Dickstein, D. P. Kingma, A. Kumar, S. Ermon, and B. Poole. Score-based generative modeling through stochastic differential equations. In *International Conference on Learning Representations*, 2021. URL <https://openreview.net/forum?id=PXTIG12RRHS>.
- O. Talagrand. Evaluation of probabilistic prediction systems. In *Workshop Proceedings" Workshop on Predictability"*, 20-22 October 1997, ECMWF, Reading, UK, 1999.
- A. Vaswani, N. Shazeer, N. Parmar, J. Uszkoreit, L. Jones, A. N. Gomez, Ł. Kaiser, and I. Polosukhin. Attention is all you need. *Advances in neural information processing systems*, 30, 2017.
- A. Weaver and P. Courtier. Correlation modelling on the sphere using a generalized diffusion equation. *Quarterly Journal of the Royal Meteorological Society*, 127(575):1815–1846, 2001.
- H. Wen, Y. Lin, Y. Xia, H. Wan, R. Zimmermann, and Y. Liang. Diffstg: Probabilistic spatio-temporal graph forecasting with denoising diffusion models. *arXiv preprint arXiv:2301.13629*, 2023.
- Wikipedia. 2019 atlantic hurricane season, Dec 2023. URL https://en.wikipedia.org/wiki/2019_Atlantic_hurricane_season.

- D. Wilks. On the reliability of the rank histogram. *Monthly Weather Review*, 139(1):311–316, 2011.
- W.M.O. *Manual on the Global Data-processing and Forecasting System*. World Meteorological Organization, 2019. ISBN 978-92-63-10485-4. URL <https://library.wmo.int/idurl/4/35703>.
- H. Yamaguchi, D. Hotta, T. Kanehama, K. Ochi, Y. Ota, R. Sekiguchi, A. Shimpo, and T. Yoshida. Introduction to jma’s new global ensemble prediction system. *CAS/JSC WGNE, Research Activities in Atmospheric and Oceanic Modelling*, 42:6–13, 2018.
- R. Yang, P. Srivastava, and S. Mandt. Diffusion probabilistic modeling for video generation. *Entropy*, 25(10):1469, 2023.
- M. Zamo and P. Naveau. Estimation of the continuous ranked probability score with limited information and applications to ensemble weather forecasts. *Mathematical Geosciences*, 50(2):209–234, 2018.
- Y. Zhang, M. Long, K. Chen, L. Xing, R. Jin, M. I. Jordan, and J. Wang. Skilful nowcasting of extreme precipitation with nowcastnet. *Nature*, 619(7970):526–532, 2023.
- Y. Zhu, Z. Toth, R. Wobus, M. Wei, and B. Cui. May 2006 upgrade of the GEFS and first implementation of naefs systems, 2012b.

Appendix

A.1. Task setup

In Section 3.1, our factorization of the conditional distribution

$$p(X^{-1:T}|O) = p(X^{-1:0}|O) \prod_{t=1}^T p(X^t|X^{t-2:t-1})$$

relies on two conditional independence assumptions. Firstly we assume that conditional on the initial states $X^{-1:0}$, future states $X^{1:T}$ are independent of initial observations O . Secondly we make a second-order Markov assumption ($p(X^t|X^{-1:t-1}) = p(X^t|X^{t-2:t-1})$ for all $t \geq 1$). These assumptions are no stronger than those made in NWP-based ensemble forecasting systems. A physical model would generally operate under a first-order Markov assumption; however given that we operate not with full physical states but with finite-resolution reconstructions of physical states, we find it advantageous to relax this to a second-order assumption so that our ML models can benefit from conditioning on additional context.

A.2. Data

A.2.1. ERA5

The following description of the ERA5 dataset is adapted directly from Lam et al. (2023). For developing GenCast, we built our datasets from a subset of ECMWF’s ERA5 Hersbach et al. (2020)⁶ archive, which is a large corpus of data that represents the global weather from 1959 to the present, at 1 hour increments, for hundreds of static, surface, and atmospheric variables. The ERA5 archive is based on *reanalysis*, which uses ECMWF’s HRES model (cycle 42r1) that was operational for most of 2016, within ECMWF’s 4D-Var data assimilation system. ERA5 assimilated 12-hour windows of observations, from 21z-09z and 09z-21z, as well as previous forecasts, into a dense representation of the weather’s state, for each historical date and time. The ERA5 archive consists of a deterministic reanalysis (ERA5) computed at 0.281 25° native latitude/longitude resolution, and an associated ensemble reanalysis (the ERA5 Ensemble of Data Assimilations or ERA5 EDA), which consists of 9 ensemble members and 1 control member computed at a lower 0.5625° native resolution.

Our ERA5 dataset contains a subset of available variables in ECMWF’s ERA5 archive (Table A.1), on 13 pressure levels⁷ corresponding to the levels of the WeatherBench (Rasp et al., 2020) benchmark: 50, 100, 150, 200, 250, 300, 400, 500, 600, 700, 850, 925, 1000 hPa. The range of years included was 1979-01-01 to 2022-01-10, which were downsampled to 12 hour time intervals (corresponding to 00z, 06z, 12z and 18z each day). The downsampling is performed by subsampling, except for the total precipitation, which is accumulated for the 12 hours leading up to the corresponding downsampled time.

Handling of ENS missing data. As found in Lam et al. (2023), an extremely small subset of the values downloaded and regridded from the ECMWF archive are not numbers (NaN). For the TIGGE ENS data this affected the variable geopotential at 250hPa. For easier comparison, we filled these rare missing values with the weighted average of the immediate neighboring pixels. We used a weight of

⁶See ERA5 documentation: <https://confluence.ecmwf.int/display/CKB/ERA5>.

⁷We follow common practice of using pressure as our vertical coordinate, instead of altitude. A “pressure level” is a field of altitudes with equal pressure. E.g., “pressure level 500 hPa” corresponds to the field of altitudes for which the pressure is 500 hPa. The relationship between pressure and altitude is determined by the geopotential variable.

1 for side-to-side neighbors and 0.5 weights for diagonal neighbors. We also got persistent errors (from both TIGGE and MARS) when trying to download ENS forecasts for surface variables for the 2019-10-17 00z initialization, so we left that initialization out of the ENS evaluation.

Variables with NaNs. ERA5 sea surface temperature (SST) data contains NaNs over land by default. As preprocessing of the SST training and evaluation data, values over land are replaced with the minimum sea surface temperature seen globally in a subset of ERA5.

Type	Variable name	Short name	ECMWF Parameter ID	Role (accumulation period, if applicable)
Atmospheric	Geopotential	z	129	Input/Predicted
Atmospheric	Specific humidity	q	133	Input/Predicted
Atmospheric	Temperature	t	130	Input/Predicted
Atmospheric	U component of wind	u	131	Input/Predicted
Atmospheric	V component of wind	v	132	Input/Predicted
Atmospheric	Vertical velocity	w	135	Input/Predicted
Single	2 metre temperature	2t	167	Input/Predicted
Single	10 metre u wind component	10u	165	Input/Predicted
Single	10 metre v wind component	10v	166	Input/Predicted
Single	Mean sea level pressure	msl	151	Input/Predicted
Single	Sea Surface Temperature	sst	34	Input/Predicted
Single	Total precipitation	tp	228	Predicted (12h)
Static	Geopotential at surface	z	129	Input
Static	Land-sea mask	lsm	172	Input
Static	Latitude	n/a	n/a	Input
Static	Longitude	n/a	n/a	Input
Clock	Local time of day	n/a	n/a	Input
Clock	Elapsed year progress	n/a	n/a	Input

Table A.1 | **ECMWF variables used in our datasets.** The “Type” column indicates whether the variable represents a *static* property, a time-varying *single*-level property (e.g., surface variables are included), or a time-varying *atmospheric* property. The “Variable name” and “Short name” columns are ECMWF’s labels. The “ECMWF Parameter ID” column is a ECMWF’s numeric label, and can be used to construct the URL for ECMWF’s description of the variable, by appending it as suffix to the following prefix, replacing “ID” with the numeric code: <https://apps.ecmwf.int/codes/grib/param-db/?id=ID>. The “Role” column indicates whether the variable is something our model takes as input and predicts, or only uses as input context (the double horizontal line separates predicted from input-only variables, to make the partitioning more visible).

A.3. Diffusion settings

A.3.1. Sampler hyperparameters

To draw samples we use DPMSolver++2S (Lu et al., 2022) as a drop-in replacement for the second-order Heun solver used in Karras et al. (2022). It is also a second-order ODE solver requiring $2N - 1$ function evaluations for N noise levels (two per step, one fewer for the final Euler step). We augment it with the stochastic churn and noise inflation described in Algorithm 2 of Karras et al. (2022).

At sampling time we adopt the noise level schedule specified by [Karras et al. \(2022\)](#):

$$\sigma_i := \left(\sigma_{\max}^{\frac{1}{\rho}} + \frac{i}{N-1} (\sigma_{\min}^{\frac{1}{\rho}} - \sigma_{\max}^{\frac{1}{\rho}}) \right)^{\rho} \quad \text{for } i \in \{0 \dots N-1\}$$

Settings for the parameters of this schedule ($\rho, \sigma_{\min}, \sigma_{\max}, N$) as well for stochastic churn and noise inflation are given in Table A.2.

Name	Notation	Value, sampling	Value, training
Maximum noise level	σ_{\max}	80	88
Minimum noise level	σ_{\min}	0.03	0.02
Shape of noise distribution	ρ	7	7
Number of noise levels	N	20	
Stochastic churn rate	S_{churn}	2.5	
Churn maximum noise level	$S_{t\max}$	80	
Churn minimum noise level	$S_{t\min}$	0.75	
Noise level inflation factor	S_{noise}	1.05	

Table A.2 | **Settings used at sampling time, and their equivalents at training time where applicable.** Notation aligns with that used in [Karras et al. \(2022\)](#).

A.3.2. Training-time noise-level distribution

At training time we construct a continuous distribution for noise levels, whose quantiles match the noise level schedule described above. Specifically its inverse CDF is:

$$F^{-1}(u) = \left(\sigma_{\max}^{\frac{1}{\rho}} + u(\sigma_{\min}^{\frac{1}{\rho}} - \sigma_{\max}^{\frac{1}{\rho}}) \right)^{\rho}$$

and we sample from it by drawing $u \sim U[0, 1]$. At training time we use the same ρ as at sampling time, but a slightly wider range for $[\sigma_{\min}, \sigma_{\max}]$, values are in Table A.2.

A.3.3. Noise distribution on the sphere

Much of the theory around diffusion models is developed for the case of Gaussian white noise. A true white noise process on the sphere is isotropic or rotation-invariant, and is characterised by a flat spherical harmonic power spectrum in expectation. However these properties do not hold if we attempt to approximate it at finite resolution by sampling i.i.d. noise on the cells of our equi-angular latitude-longitude grid. This is due to the greater density of cells near to the poles which results in more power at higher frequencies in the spherical harmonic domain.

Empirically we didn't find this to be a fatal problem; nonetheless we found we can obtain a small but consistent improvement using a different approach to noise sampling which is sensitive to the spherical geometry. We sample isotropic Gaussian noise in the spherical harmonic domain, with an expected power spectrum that is flat over the range of wavenumbers that our grid is able to resolve, and truncated thereafter. We then project it onto our discrete grid using the inverse spherical harmonic transform ([Driscoll and Healy, 1994](#)). The resulting per-grid-cell noise values are not independent especially near to the poles, but are approximately independent at the resolution resolved at the equator, and display the desired properties of isotropy and flat power spectrum.

A.4. Initial conditions

We explored a number of methods for deriving ensemble initial conditions for our ML models. In this section we discuss these methods in more detail in order to motivate the choices we made. We also supply full details of the ad-hoc Gaussian Process perturbations described in Section 4.1.2.

A.4.1. Deterministic analysis

We tried initializing every ensemble member in the same way, using two consecutive deterministic analyses from ECMWF’s ERA5 reanalysis dataset. This is a relatively crude approximation as it collapses initial condition uncertainty down to a pair of point estimates. A deterministic model initialized this way will have no dispersion, but the method works relatively well for our diffusion model.

A.4.2. Ensemble of data assimilations (EDA) analysis

Another possibility is to initialize each ensemble member using two consecutive ensemble analyses from a corresponding ensemble member of ECMWF’s ERA5 EDA. This better approximates a posterior distribution conditional on observations. However it still tends to be under-dispersed (Buizza et al., 2008), and the ERA5 EDA was computed using IFS at half the native resolution used for ERA5 itself (Hersbach et al., 2020), reducing the quality of the analysis.

A.4.3. Deterministic analysis plus EDA perturbations

Following ECMWF (Buizza et al., 2008) we combine the high quality of the deterministic analysis with the distributional information of the ensemble analysis, by taking the deterministic ERA5 analysis and adding to it perturbations equal to the difference between ERA5 EDA members and their mean. This is analogous to the use of EDA perturbations in initializing ECMWF’s ENS forecast system, although we do not include the additional singular value perturbations used at ECMWF to address under-dispersion of the EDA perturbations, largely because we were not easily able to obtain singular value perturbations for use with the ERA5 EDA dataset. Nevertheless this method yielded the best results for our diffusion model.

A.4.4. Deterministic analysis plus EDA perturbations and ad-hoc Gaussian process perturbations

The final method we explored takes the deterministic ERA5 analysis with EDA perturbations and adds to it perturbations sampled from a zero-mean Gaussian process on the sphere. This process uses the Gaussian-like stationary isotropic correlation function from Weaver and Courtier (2001), with a horizontal decorrelation length-scale of 1200km.

Geopotential
Temperature
U component of wind
V component of wind
2-metre temperature

Table A.3 | Variables to which Gaussian process perturbations are applied

We sample independent perturbations for each of the variables listed in Table A.3; other variables are not perturbed by the Gaussian process. We obtained better results perturbing only this subset than the full set of input variables, although we have not exhaustively investigated the best subset of variables to perturb.

The marginal standard deviations of the perturbations are equal to 0.085 times those of 6-hour differences in the corresponding variables at each respective pressure (or surface) level. Aside from these differences in scale, for a given variable the same perturbation is used for all levels, and for both input timesteps. This is equivalent to infinite vertical and temporal decorrelation lengthscales. We investigated using lower vertical decorrelation lengthscales but found they did not help.

We selected the scale factor 0.085 and horizontal decorrelation length-scale 1200km based on CRPS scores for the resulting forecasts over a range of variables and lead times, after sweeping over scale factors (0.03, 0.05, 0.07, 0.085, 0.1, 0.3), and decorrelation length-scales (30km, 480km, 1200km, 3000km). Results were significantly worse at the shortest lengthscale we tried of 30km, but were not otherwise very sensitive to decorrelation lengthscale.

These perturbations are quite crude; in particular they are not flow-dependent and do not take any care to preserve physical invariants. Nevertheless we’ve found them to be surprisingly effective at longer lead times with the deterministic GraphCast model. In combination with EDA perturbations, they appear to play a similar role to the singular value perturbations used operationally at ECMWF to address the under-dispersion of EDA perturbations. They also allow us to generate ensembles of arbitrary size from deterministic GraphCast, without being limited by the size of the EDA ensemble. However as noted, with the diffusion model they do not give any additional skill over EDA perturbations alone, in fact for the diffusion model, skill is reduced when these perturbations are added with all but the smallest scale factors.

A.5. Optimizer hyperparameters

Optimiser	AdamW (Loshchilov and Hutter, 2018)	Weight decay	0.1
Warm-up steps	1e3	Total train steps	2e6
Peak LR	1e-3	LR decay schedule	Cosine

Table A.4 | Diffusion model training hyperparameters.

A.6. Verification metrics

In the following,

- $x_{i,m}^n$ denotes the value of the n th of N ensemble members on the m th of M forecasts for a particular variable, level and lead time, at latitude and longitude indexed by $i \in G$.
- $y_{i,m}$ denotes the corresponding verification target.
- $\bar{x}_{i,m} = \frac{1}{N} \sum_n x_{i,m}^n$ denotes the ensemble mean.
- a_i denotes the area of the latitude-longitude grid cell, which varies by latitude and is normalized to unit mean over the grid.

A.6.1. CRPS

The Continuous Ranked Probability Score (CRPS, see e.g. Gneiting and Raftery (2007)) is estimated for our ensembles as follows:

$$\text{CRPS} := \frac{1}{M} \sum_m \frac{1}{|G|} \sum_i a_i \left(\frac{1}{N} \sum_n |x_{i,m}^n - y_{i,m}| - \frac{1}{2N^2} \sum_{n,n'} |x_{i,m}^n - x_{i,m}^{n'}| \right) \quad (\text{A.1})$$

Here we use the traditional estimator of CRPS, which estimates the expected CRPS of the empirical distribution of a finite ensemble of size N .

An alternative is the ‘fair’ CRPS estimator (Zamo and Naveau, 2018), which estimates the CRPS that would be attained in the limit of an infinite ensemble. In our case this would not be appropriate as we make use of precomputed NWP ensemble analyses of finite size, and we do not wish to assume that they can be scaled up arbitrarily. Although we can scale up our own ensembles relatively cheaply, in doing so we must repeatedly re-use the same set of NWP ensemble analysis members, and the fair CRPS estimator would not correctly model this re-use.

A.6.2. Brier score

We compute Brier scores for the exceedance of thresholds $T_{i,m}$, which are set relative to specified climatological percentiles. Brier scores are defined as follows, in terms of the empirical predictive probabilities $p_{i,m}^x$ of the ensembles, and indicators $p_{i,m}^y$ of the target events:

$$p_{i,m}^x := \frac{1}{N} \sum_n \mathbb{I}[x_{i,m}^n > T_{i,m}] \quad (\text{A.2})$$

$$p_{i,m}^y := \mathbb{I}[y_{i,m} > T_{i,m}] \quad (\text{A.3})$$

$$\text{BrierScore} := \frac{1}{M} \sum_m \frac{1}{|G|} \sum_i a_i \left(p_{i,m}^x - p_{i,m}^y \right)^2 \quad (\text{A.4})$$

As with CRPS this is chosen to score the empirical probabilities of an ensemble of a specific finite size. While estimators exist for the Brier score attained by the true underlying probability of an infinite ensemble, these are not appropriate in our case for the same reason described above.

A.6.3. Ensemble mean RMSE

This is defined as:

$$\text{EnsembleMeanRMSE} := \sqrt{\frac{1}{M} \sum_m \frac{1}{|G|} \sum_i a_i (y_{i,m} - \bar{x}_{i,m})^2}. \quad (\text{A.5})$$

A.6.4. Spread/skill ratio

Following Fortin et al. (2014) we define spread as the root mean estimate of ensemble variance given below, and skill as the Ensemble-Mean RMSE from Equation (A.5):

$$\text{Spread} := \sqrt{\frac{1}{M} \sum_m \frac{1}{|G|} \sum_i a_i \frac{1}{N-1} \sum_n \left(x_{i,m}^n - \bar{x}_{i,m} \right)^2}, \quad (\text{A.6})$$

$$\text{Skill} := \text{EnsembleMeanRMSE}. \quad (\text{A.7})$$

Under these definitions and the assumption of a perfect forecast where ensemble members and ground truth $\{x_{i,m}^1, \dots, x_{i,m}^N, y_{i,m}\}$ are all exchangeable, Fortin et al. (2014) Equation 15 shows that

$$\text{Skill} \approx \sqrt{\frac{N+1}{N}} \text{Spread}, \quad (\text{A.8})$$

which motivates the following definition of spread/skill ratio including a correction for ensemble size:

$$\text{SpreadSkillRatio} := \sqrt{\frac{N+1}{N}} \frac{\text{Spread}}{\text{Skill}}. \quad (\text{A.9})$$

Under the perfect forecast assumption then, we expect to see $\text{SpreadSkillRatio} \approx 1$.

A.7. Supplementary Results and Figures

A.7.1. Results on Precipitation

In line with the rest of the paper, we evaluate precipitation forecasting skill using RMSE, CRPS and Brier scores. Since some of these metrics may not be representative of actual skill due to precipitation being highly sparse and very non-Gaussian, we also evaluated it using Stable Equitable Error in Probability Space (SEEPS) (Haiden et al., 2012; North et al., 2013; Rodwell et al., 2010), using the same methodology as in Lam et al. (2022). Because SEEPS is a metric for deterministic categorical forecasts (dry, light-rain, and heavy-rain) we evaluated the ensembles both computing the category of the ensemble mean, as well as the mode of the ensemble category members (i.e. majority vote). We repeat the caveats mentioned in the main text that we lack full confidence in the quality of ERA5 precipitation data, and that we have not tailored our evaluation to precipitation specifically beyond adding SEEPS as a further metric. Results for 12h and 24h accumulated precipitation are shown in Figure A.1 and Figure A.2 respectively.

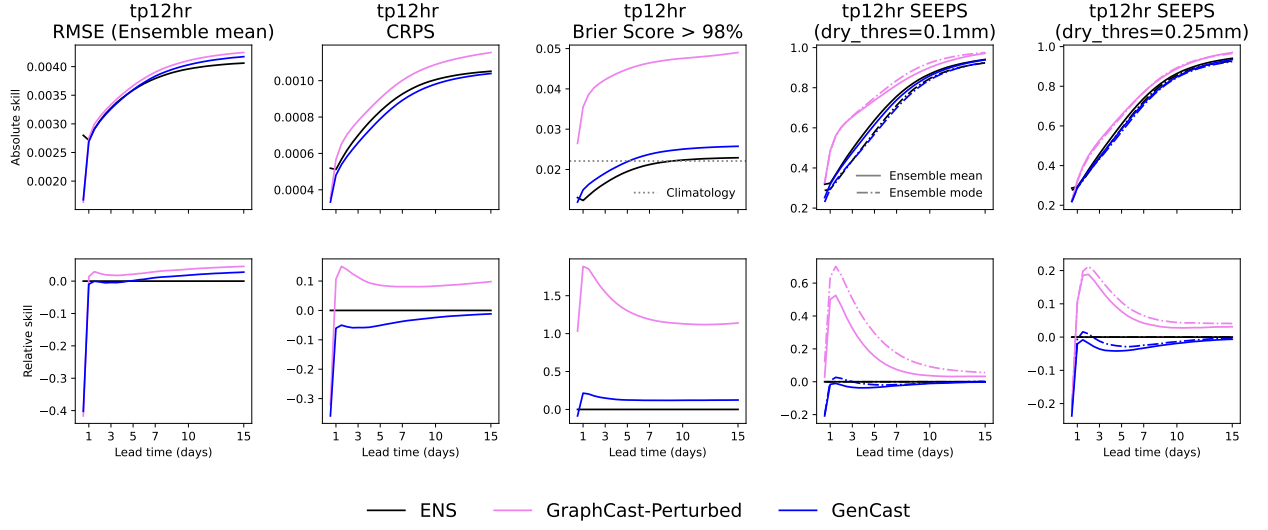


Figure A.1 | Comparing preliminary results of model performance on predicted total accumulated precipitation over 12h, evaluated on Ensemble-Mean RMSE, CRPS, Brier score for >98th percentile, and SEEPS with dry thresholds 0.1 and 0.25. All metrics were calculated globally and over the full test period, except for SEEPS which excludes very dry regions according to the criteria in [Lam et al. \(2022\)](#). For ensembles, we evaluate SEEPS both on the mean of the ensemble, as well as using the mode of the dry, light-rain, and heavy-rain categories predicted by the different ensemble members (i.e. majority vote). Relative and absolute plots are shown in the top and bottom rows respectively. GenCast shows promising results, more often than not outperforming ENS, with the exception of the Brier score, on which it is consistently outperformed by ENS.

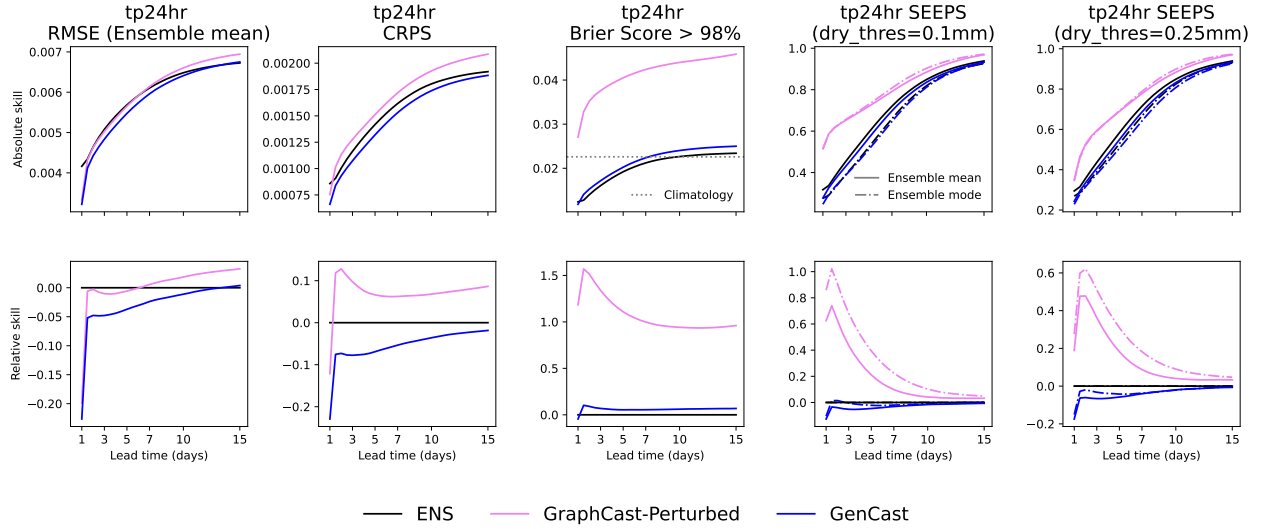


Figure A.2 | Results analogous to Figure A.1 on 24h precipitation.

A.7.2. Extended results figures

We provide additional results and figures to supplement those the main paper, showing 10 representative variables: z500, z850, q700, q925, t850, t300, u850, 2t, 10u and msl. We also provide additional scorecards to show additional model comparisons as well as to justify some verification choices.

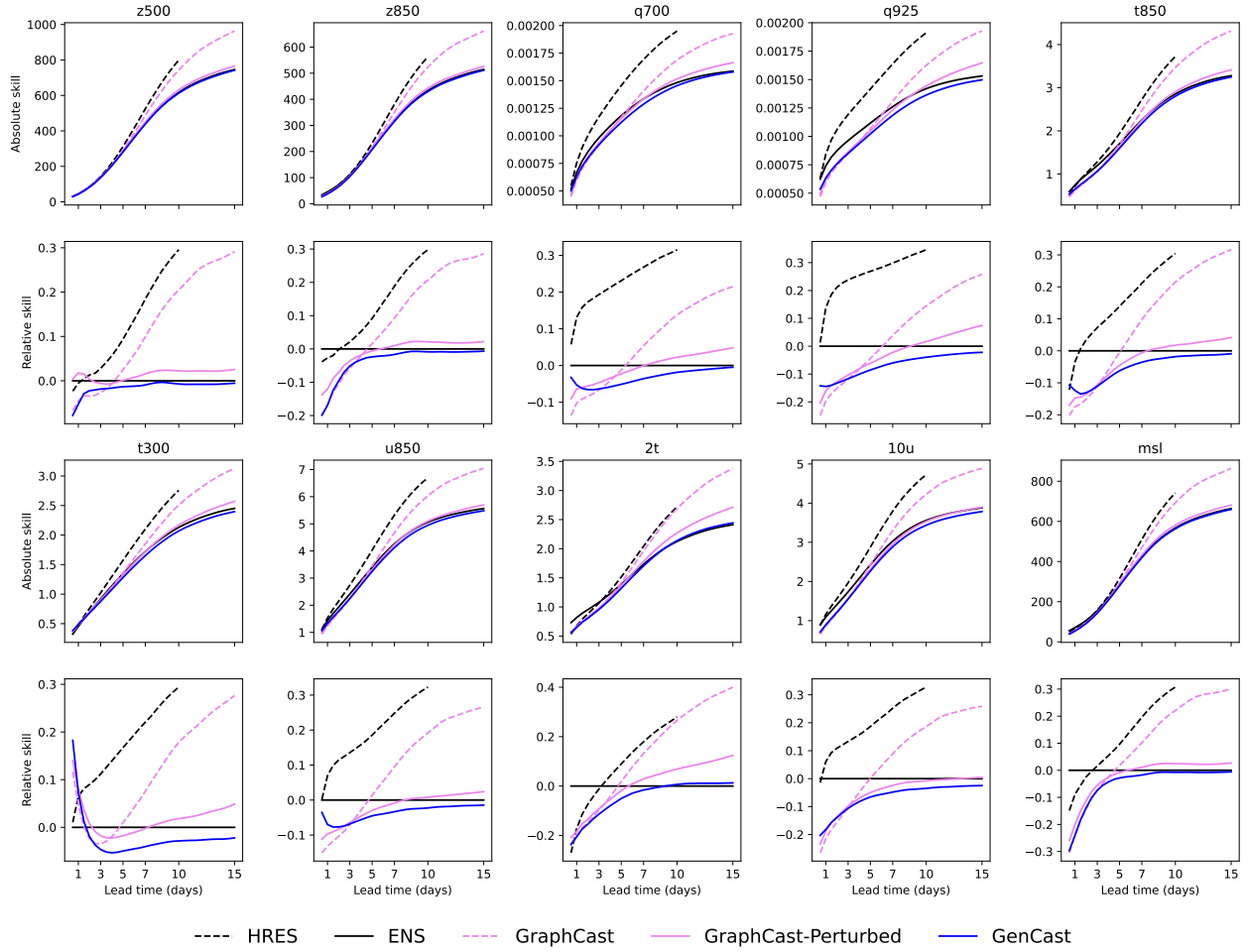


Figure A.3 | Absolute and relative RMSE (Ensemble mean) model comparison for z500, z850, q700, q925, t850, t300, u850, 2t, 10u and msl.

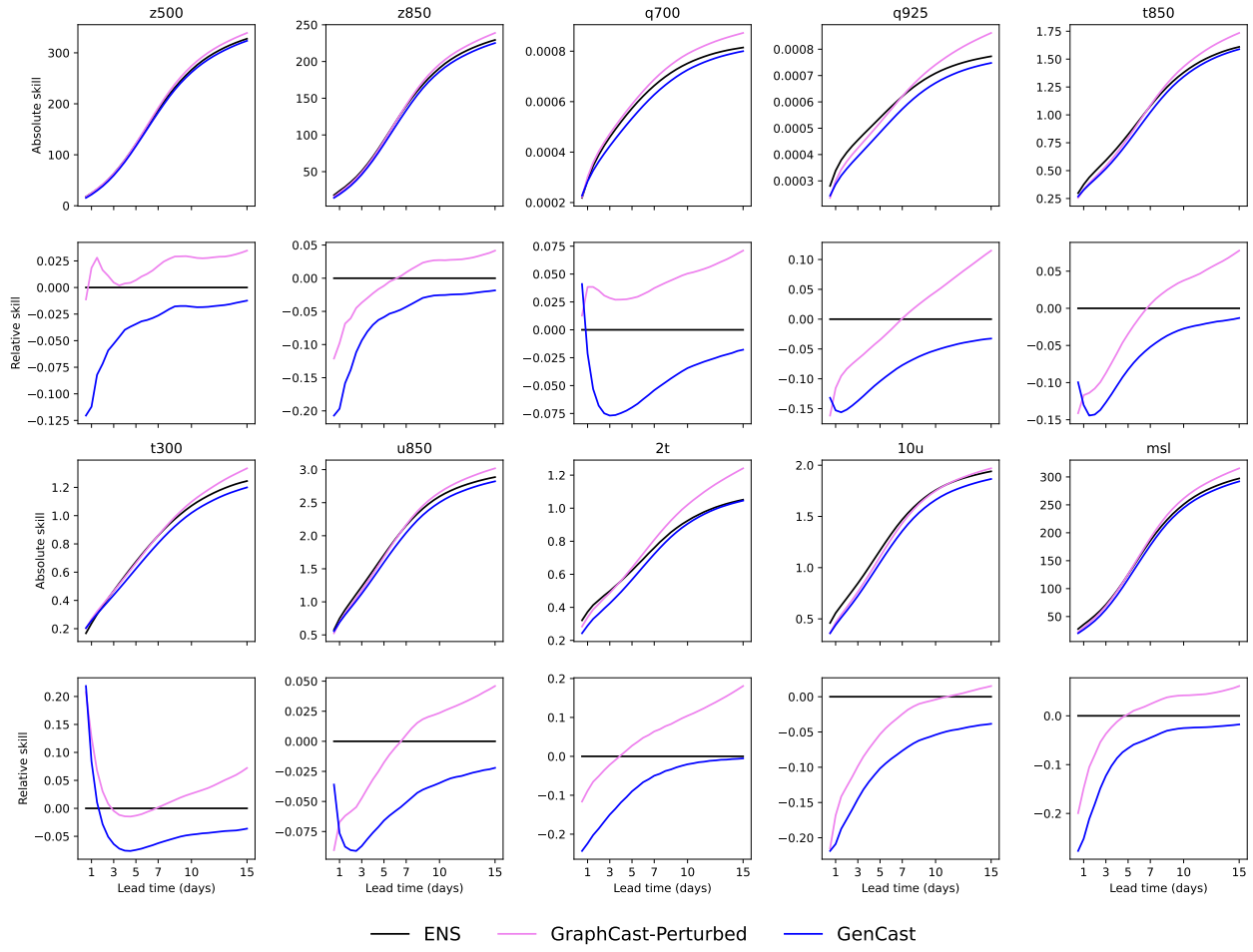


Figure A.4 | Absolute and relative CRPS model comparison for z500, z850, q700, q925, t850, t300, u850, 2t, 10u and msl.

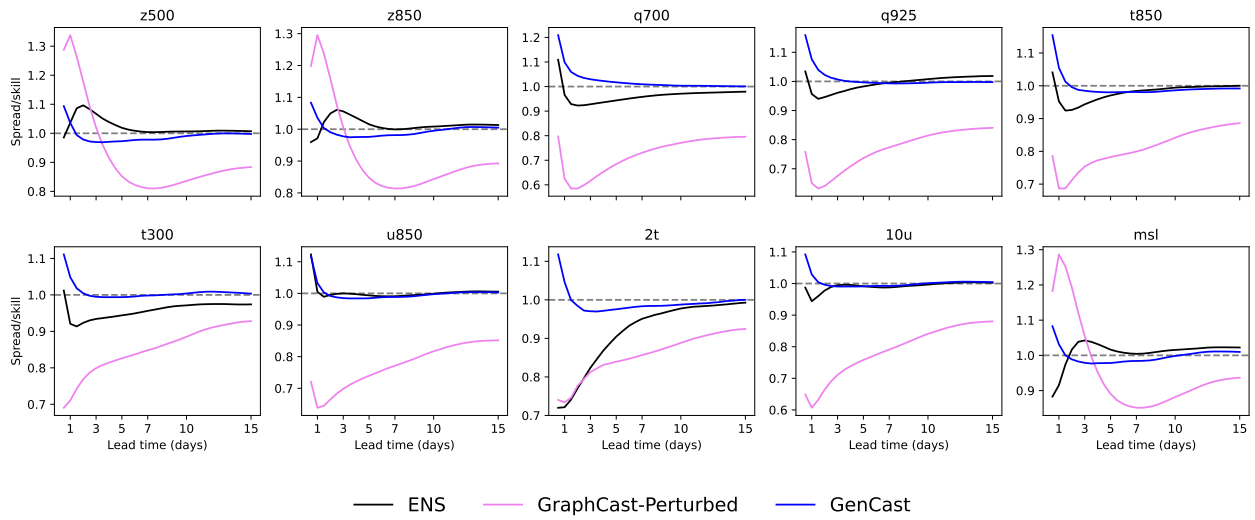


Figure A.5 | Spread/skill ratio model comparison for z500, z850, q700, q925, t850, t300, u850, 2t, 10u and msl.

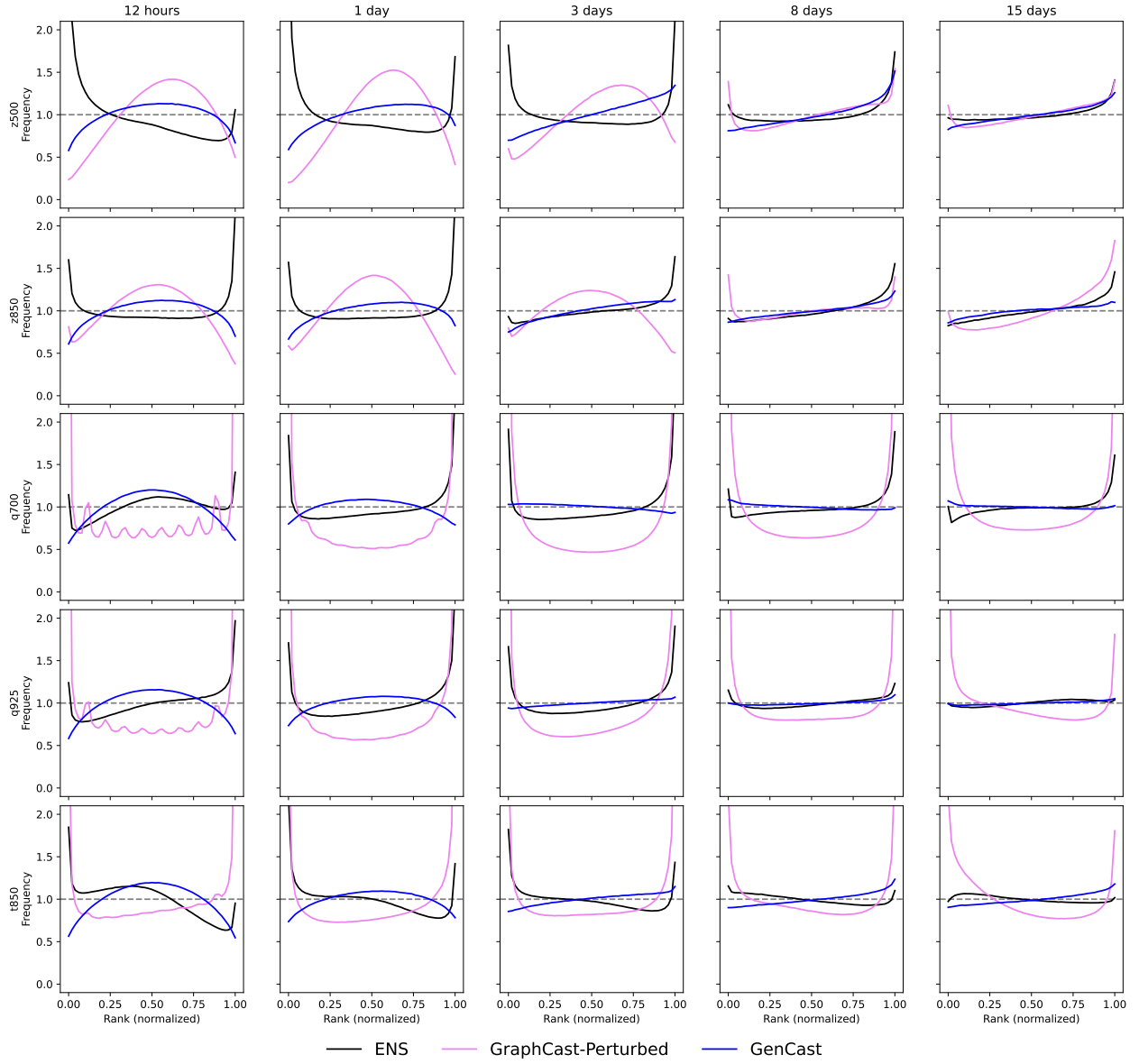


Figure A.6 | Rank histogram model comparison for z500, z850, q700, q925 and t850.

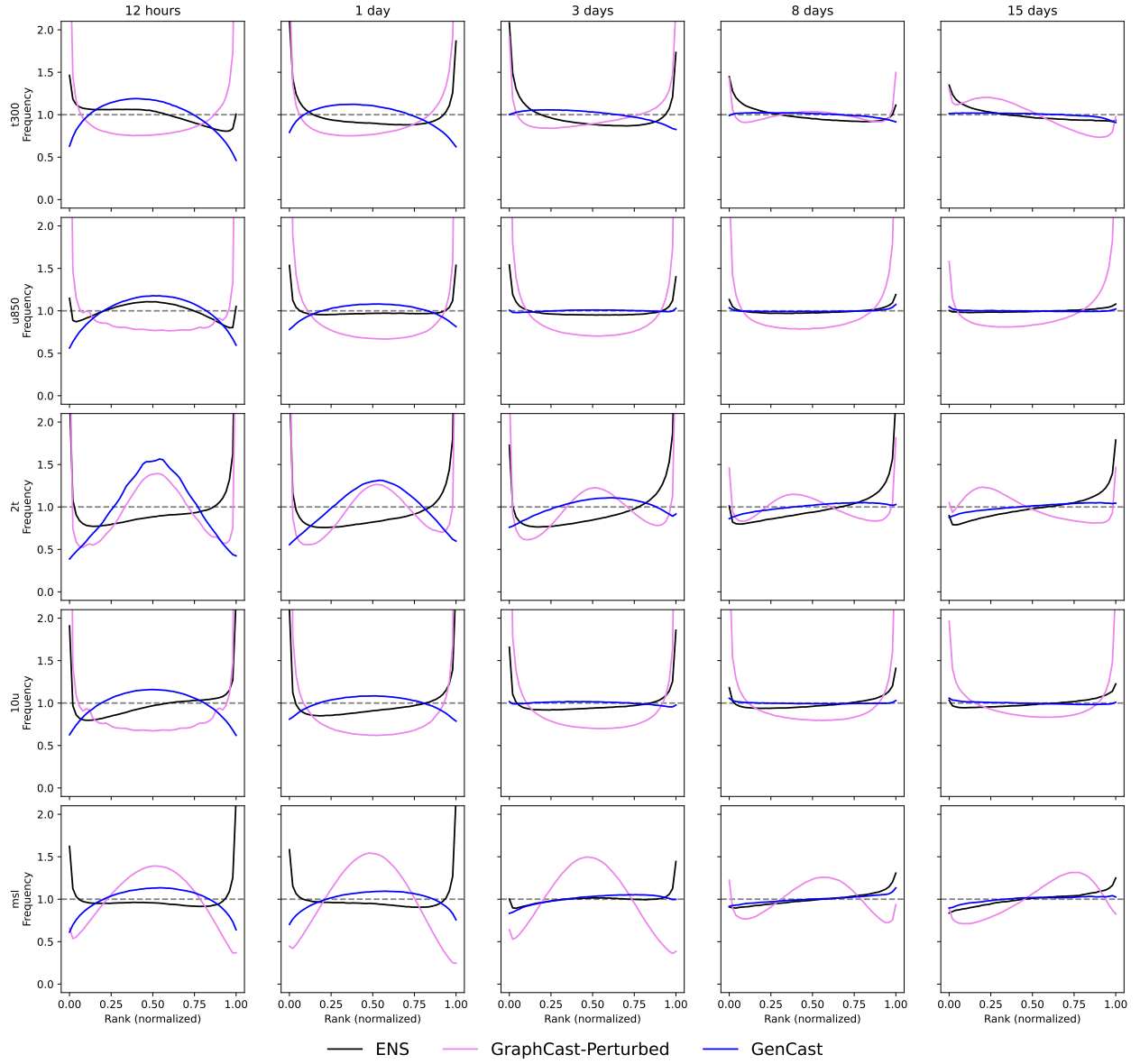


Figure A.7 | Rank histograms model comparison for t300, u850, 2t, 10u and msl.

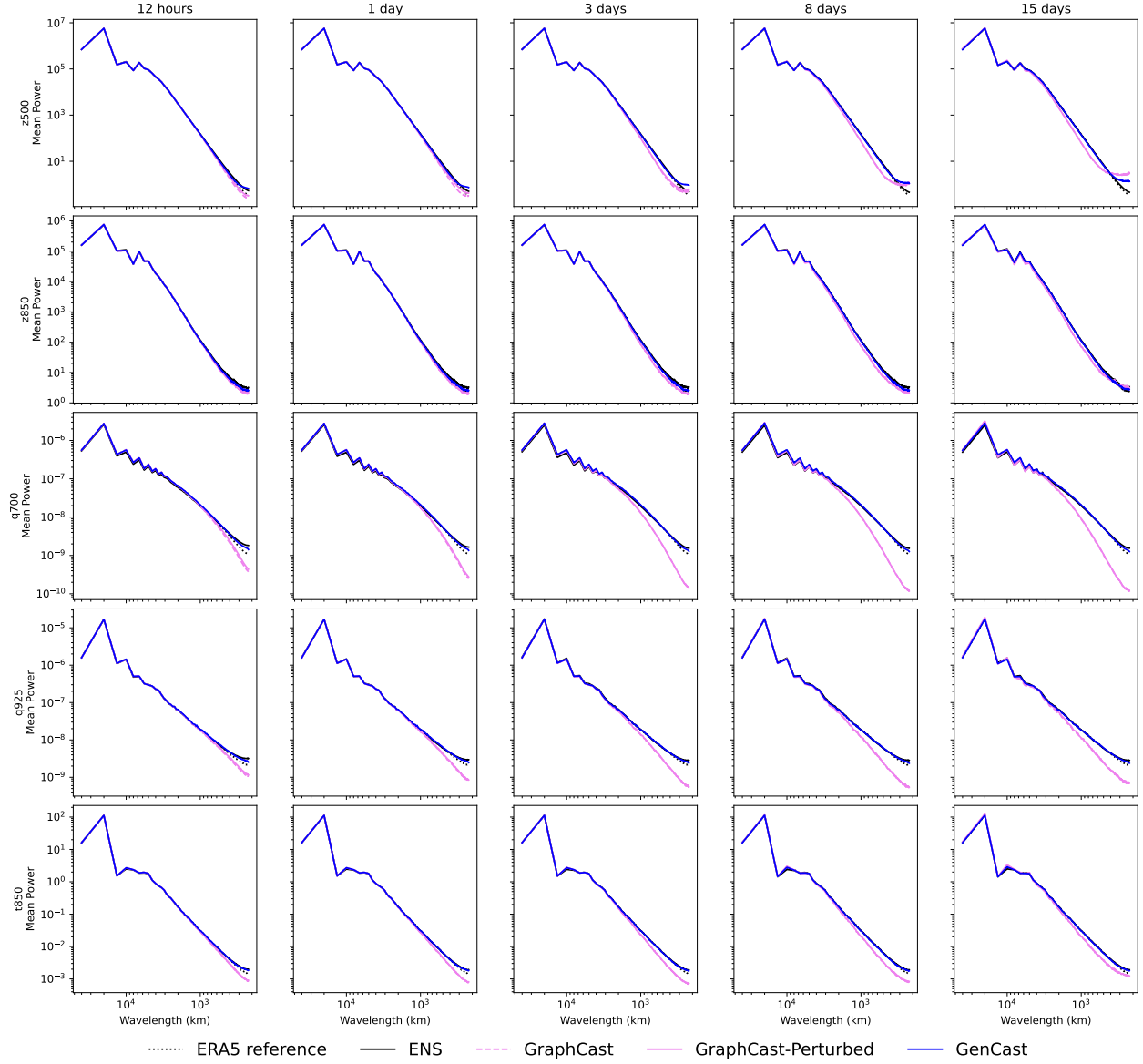


Figure A.8 | Power spectrum plots for z500, z850, q700, q925 and t850.

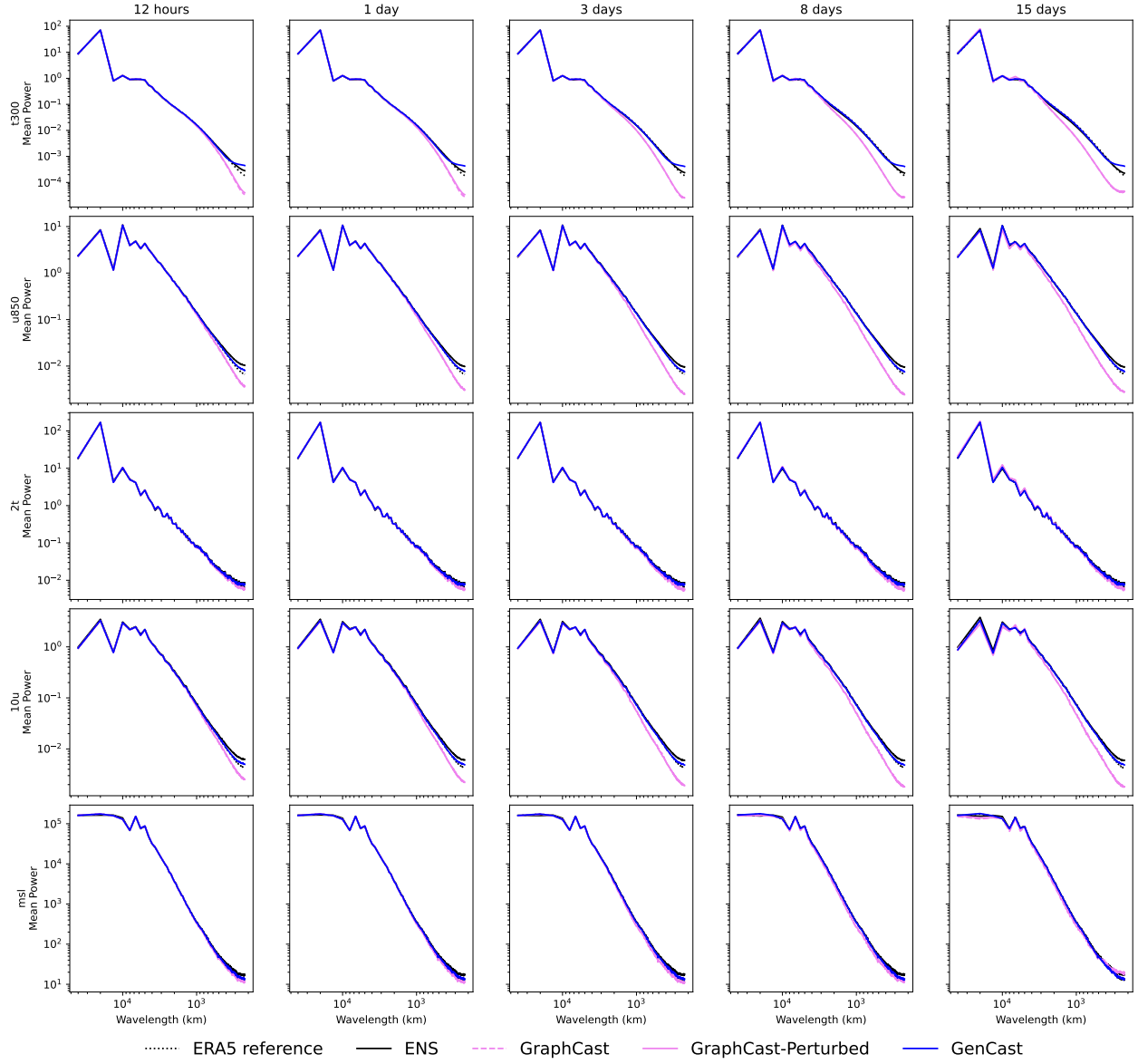


Figure A.9 | Power spectrum plots for t300, u850, 2t, 10u and msl.

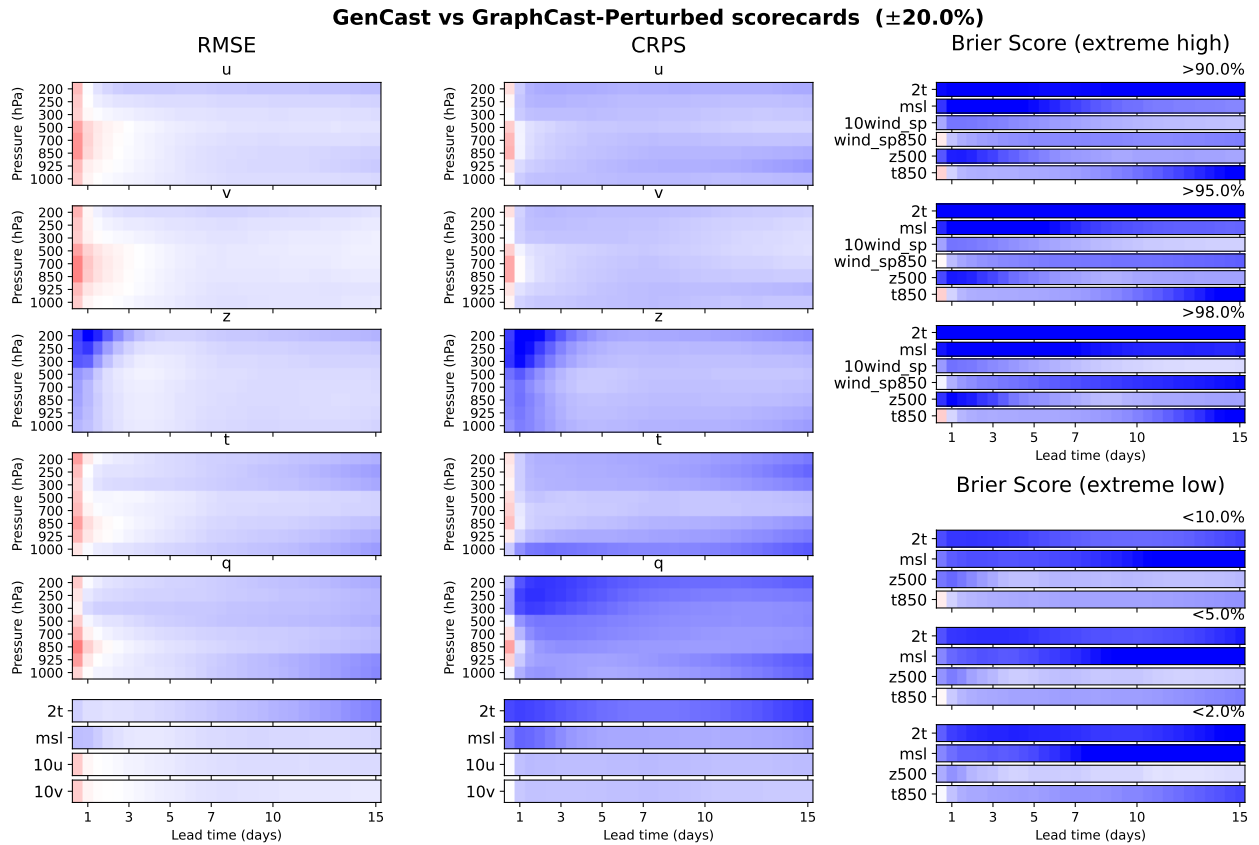


Figure A.10 | Scorecard similar to Figure 2(d-f) but comparing GenCast to GraphCast-Perturbed. The scorecard shows that GenCast dominates over longer lead times (>2 days). For very short lead times (under 1 or 2 days) GraphCast-Perturbed seems to produce better results.

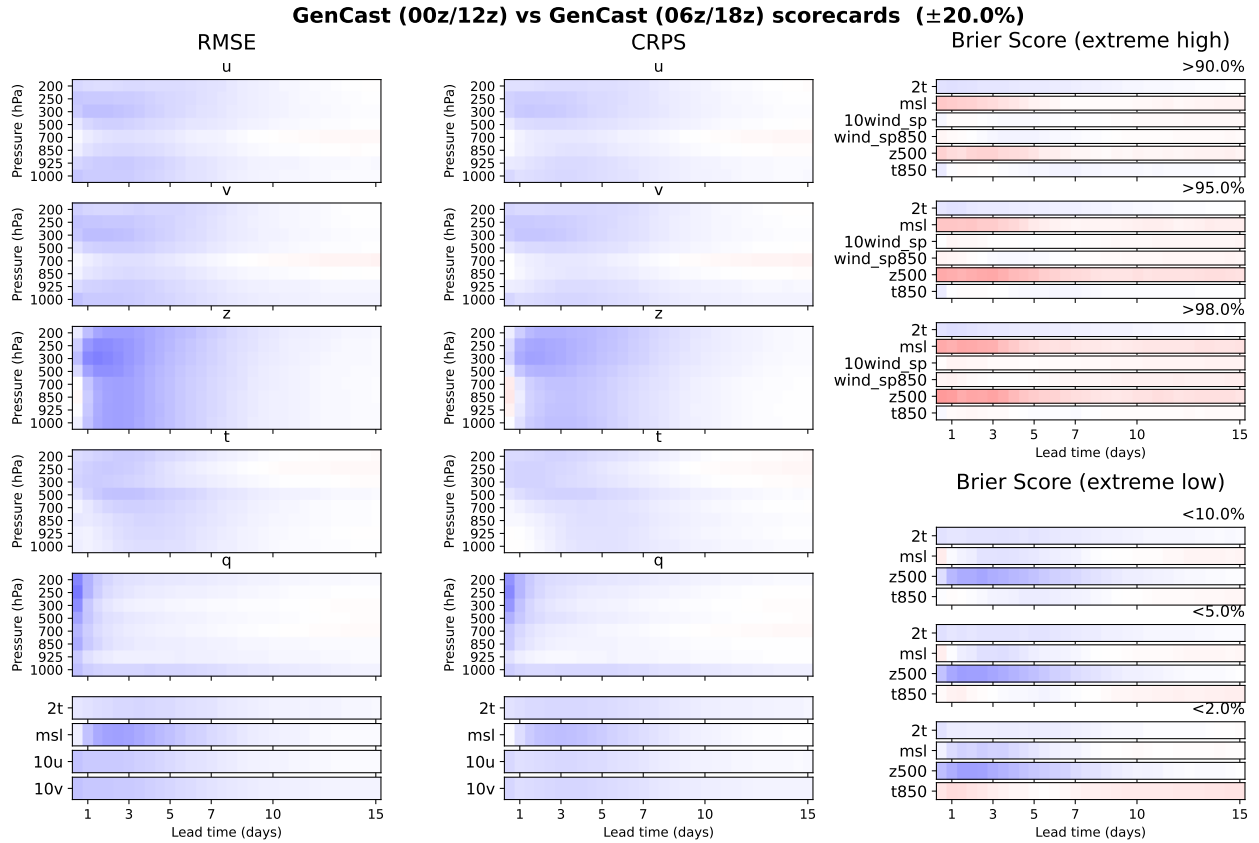


Figure A.11 | Scorecard comparing the performance of GenCast evaluated on 00z/12z initialization times, to GenCast evaluated on the 06z/18z initialization times (the latter is used in the rest of the evaluation in the paper). The 9h assimilation look-ahead of the 00z/12z initializations gives the model a consistent advantage in CRPS and Ensemble-Mean RMSE over the 3h assimilation look-ahead of the 06z/18z initializations. This highlights the importance of accounting for assimilation window look-ahead when comparing metrics across model evaluations.

A.8. Forecast visualizations

We provide forecast visualizations for 10 representative variables $z500$, $z850$, $q700$, $q925$, $t850$, $t300$, $u850$, $2t$, $10u$ and msl for the same forecast target date-time. We chose to visualize them largely over the ocean due to its flat orography, which makes it more challenging for models to preserve high frequency content. We show predictions for 2019-09-29 at 18:00:00, which overlaps with hurricane Lorenzo, one of the only two category 5 hurricanes over the Atlantic in 2019. We did not in any way cherry pick this date based on the forecasts of the model: we simply found dates for category 5 hurricanes over the Atlantic ([Wikipedia, 2023](#)), picked an approximate date overlapping with one of them, and at the time of writing this is the only forecast that we have ever visualized from the 2019 test year.

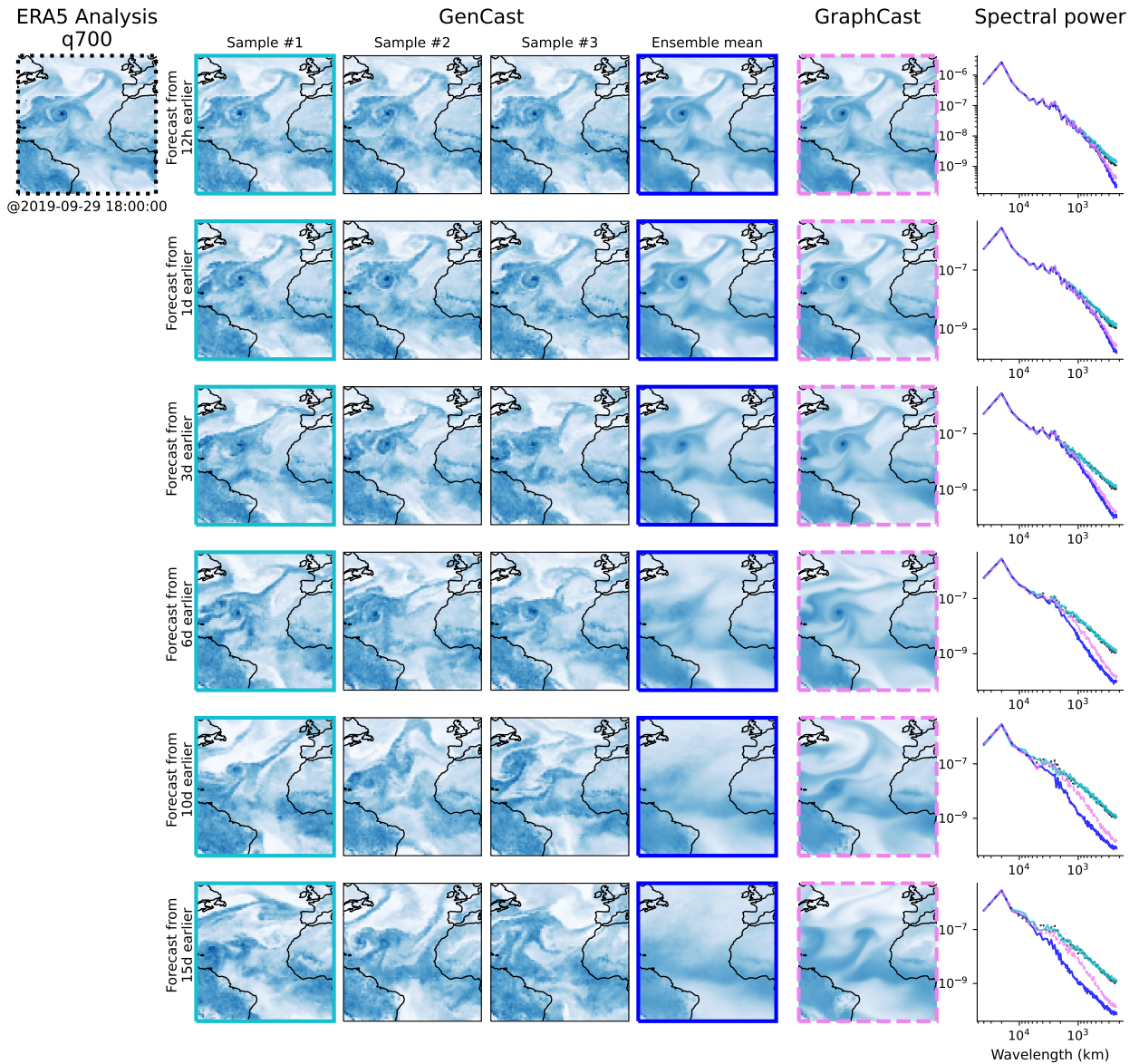


Figure A.12 | Visualization of $q700$.

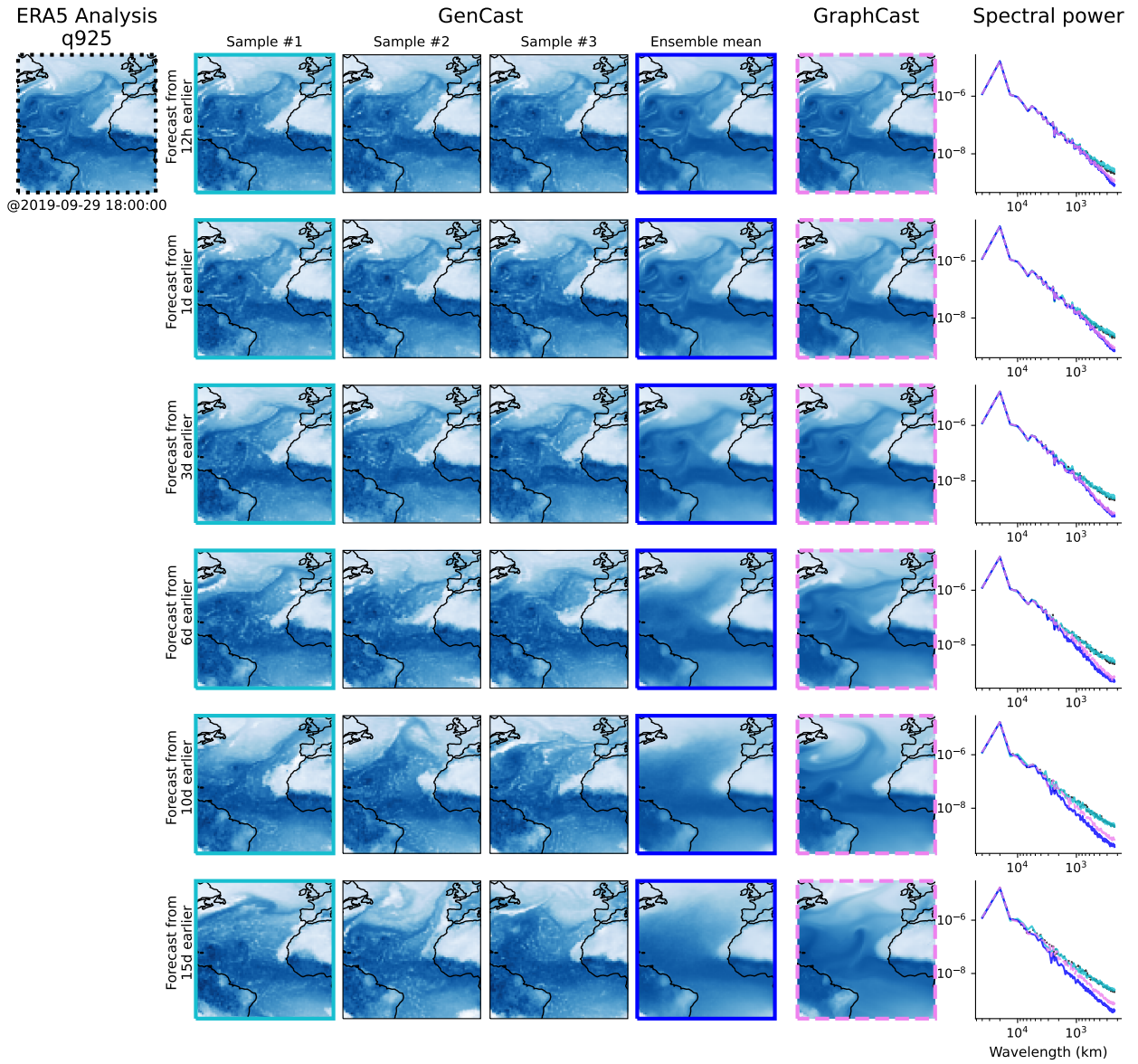


Figure A.13 | Visualization of q925.

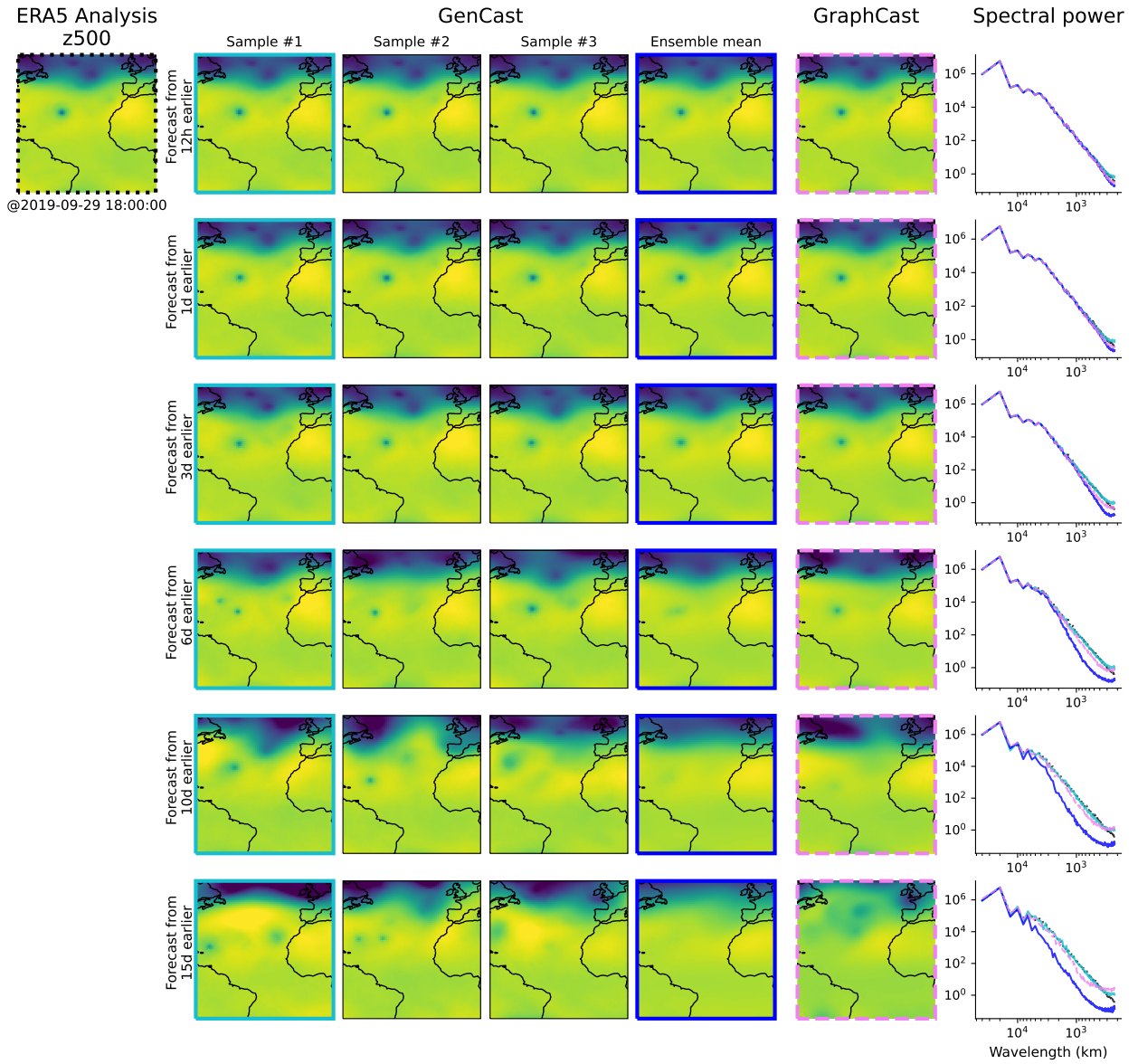


Figure A.14 | Visualization of z500.

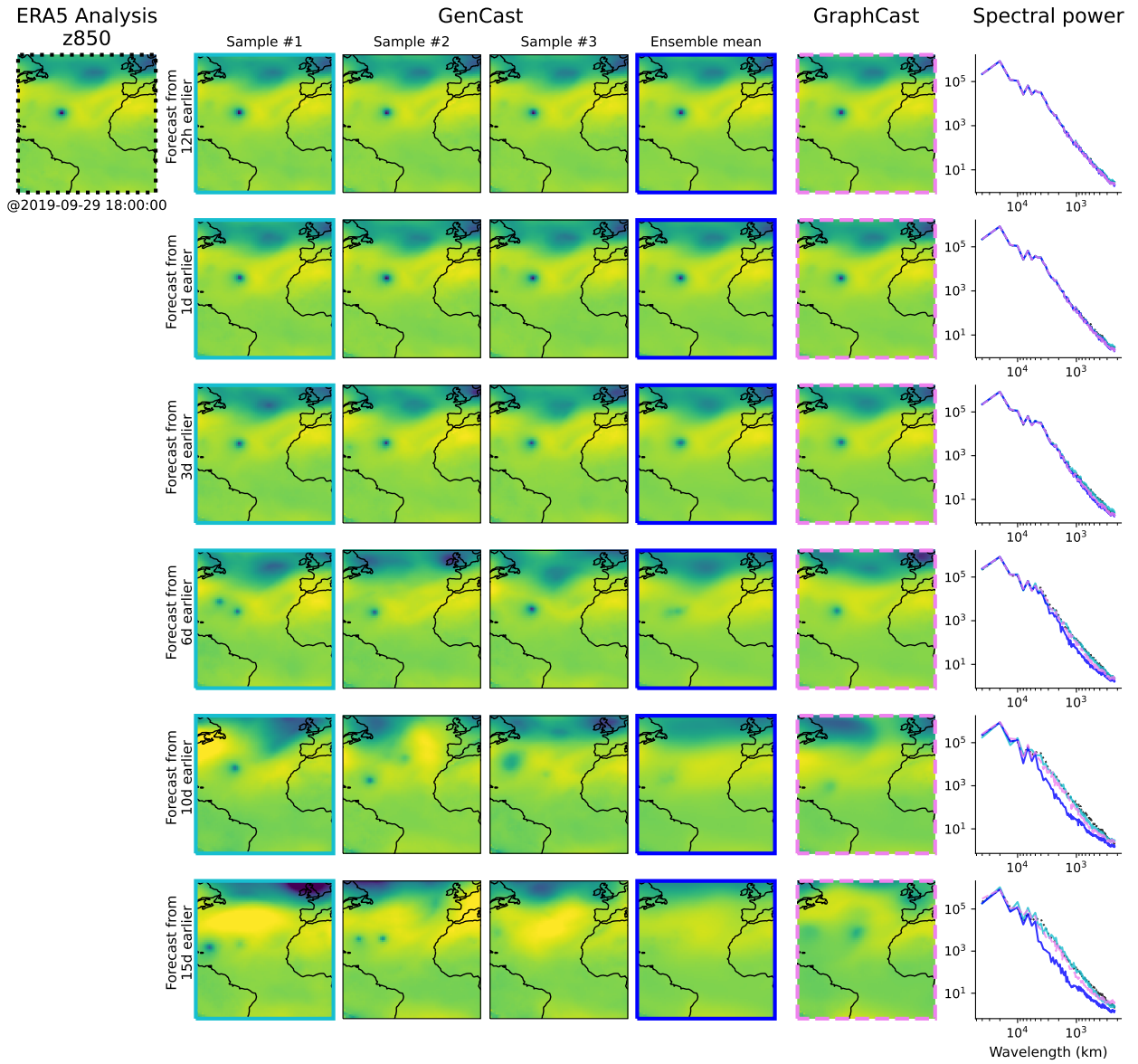


Figure A.15 | Visualization of z850.

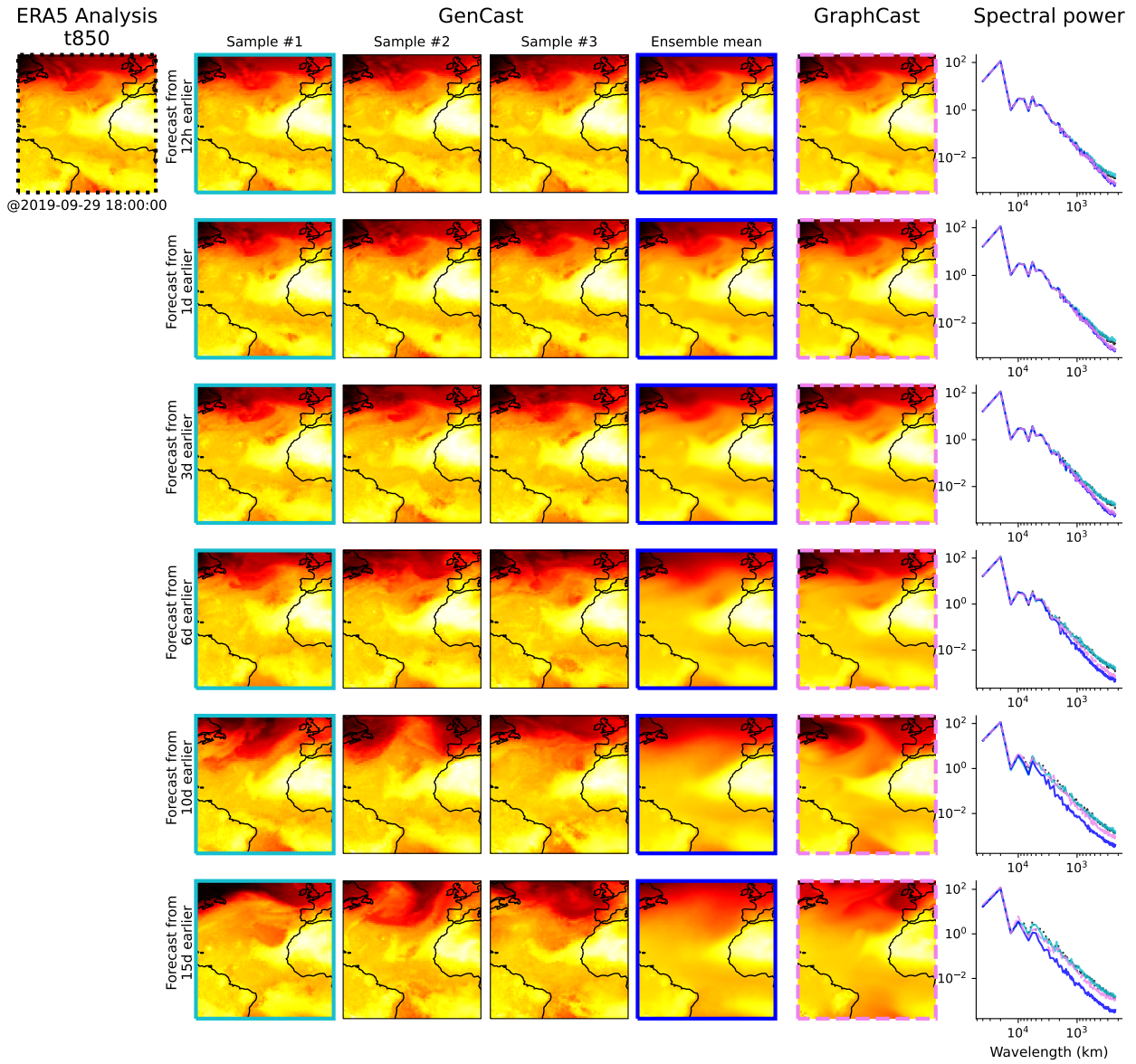


Figure A.16 | Visualization of t850.

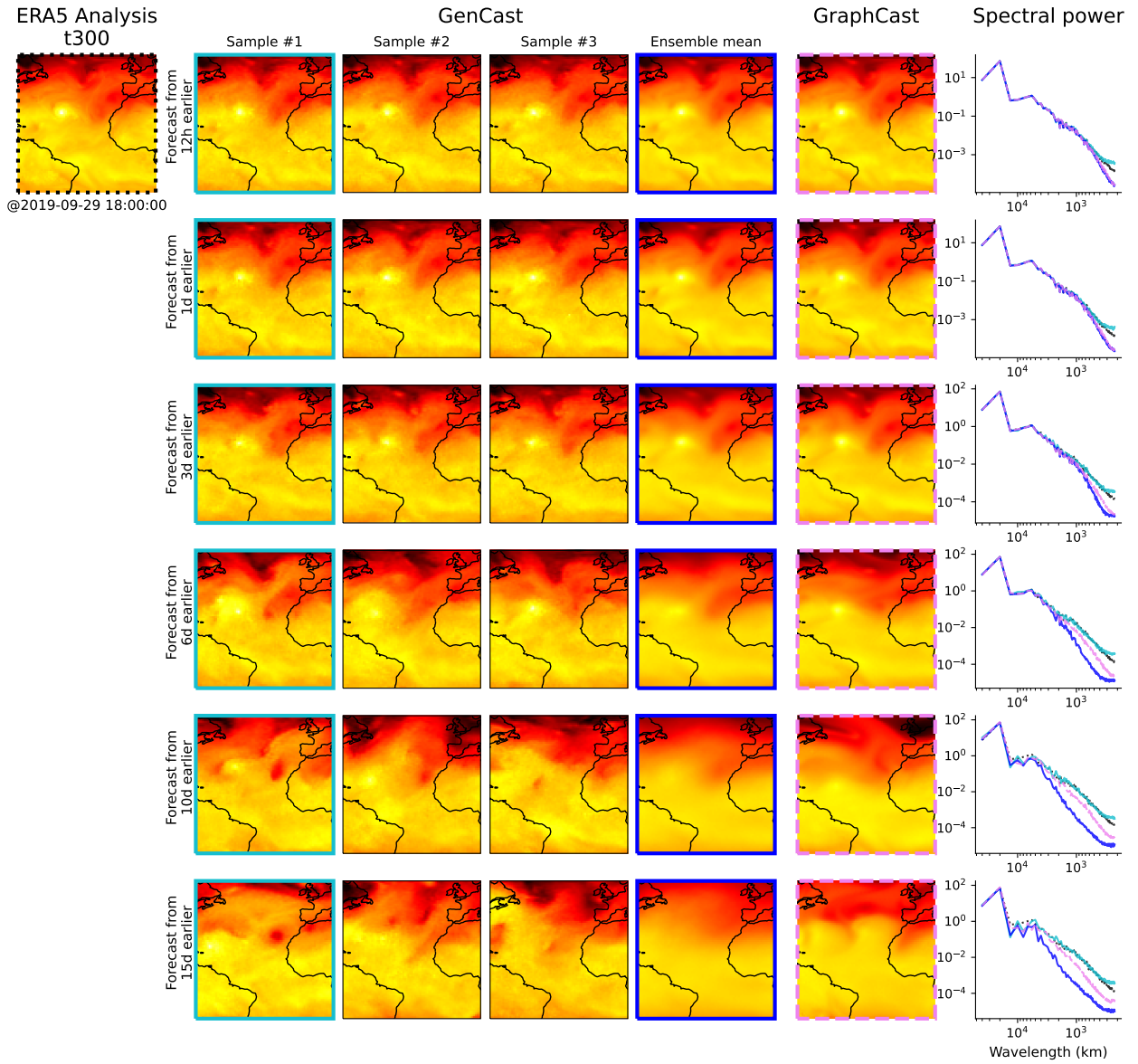


Figure A.17 | Visualization of t300.

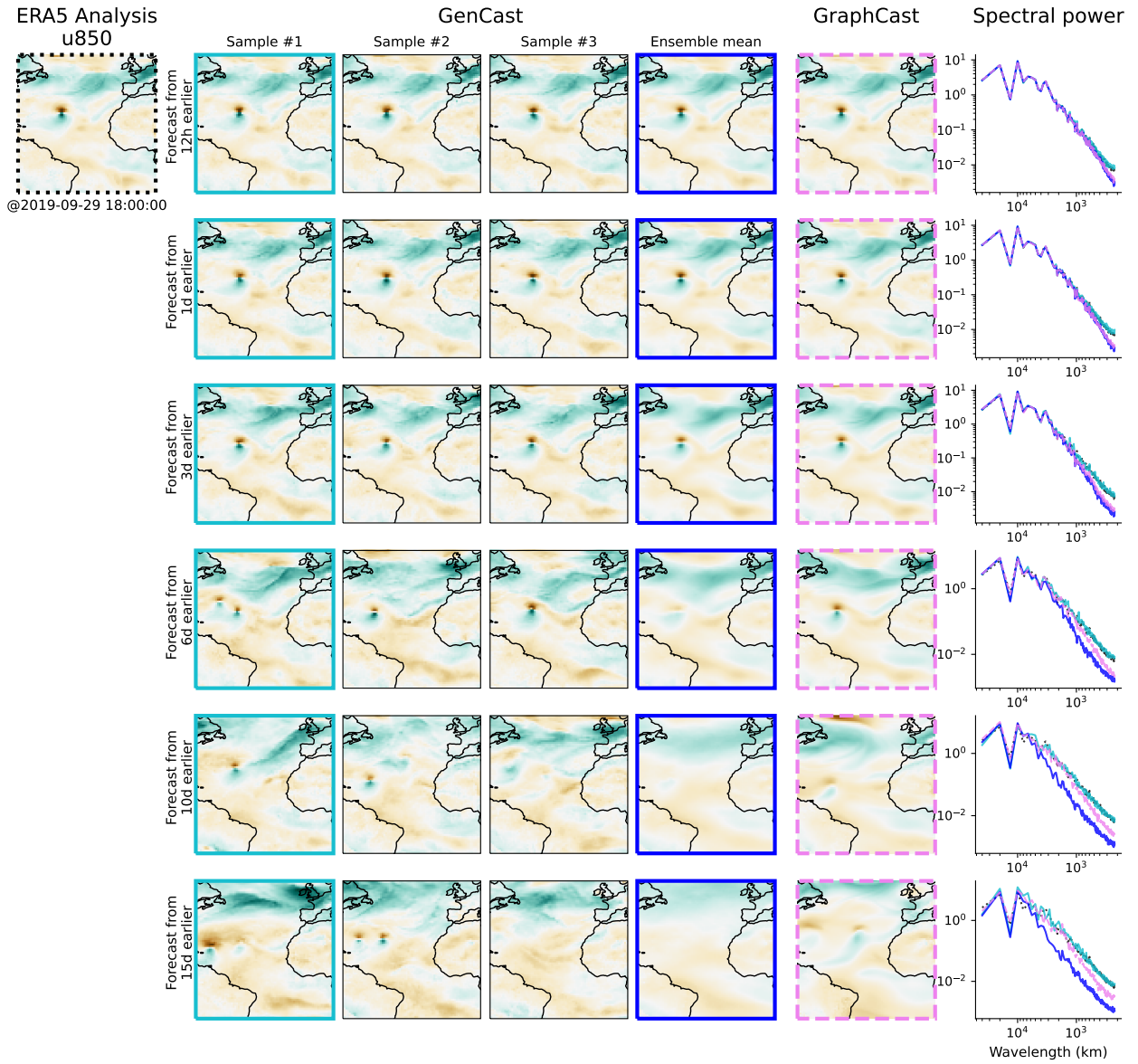


Figure A.18 | Visualization of u850.

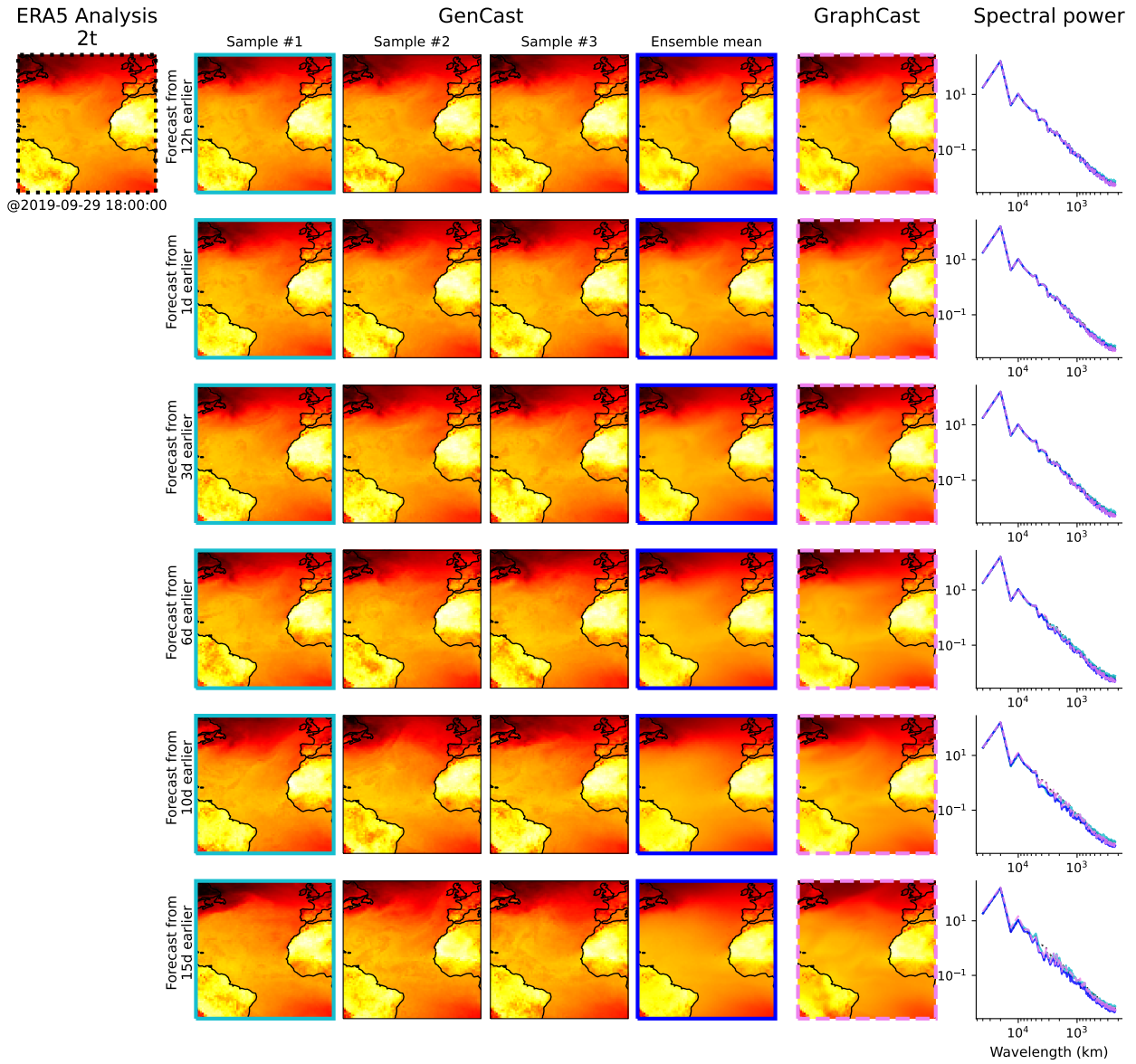


Figure A.19 | Visualization of 2t.

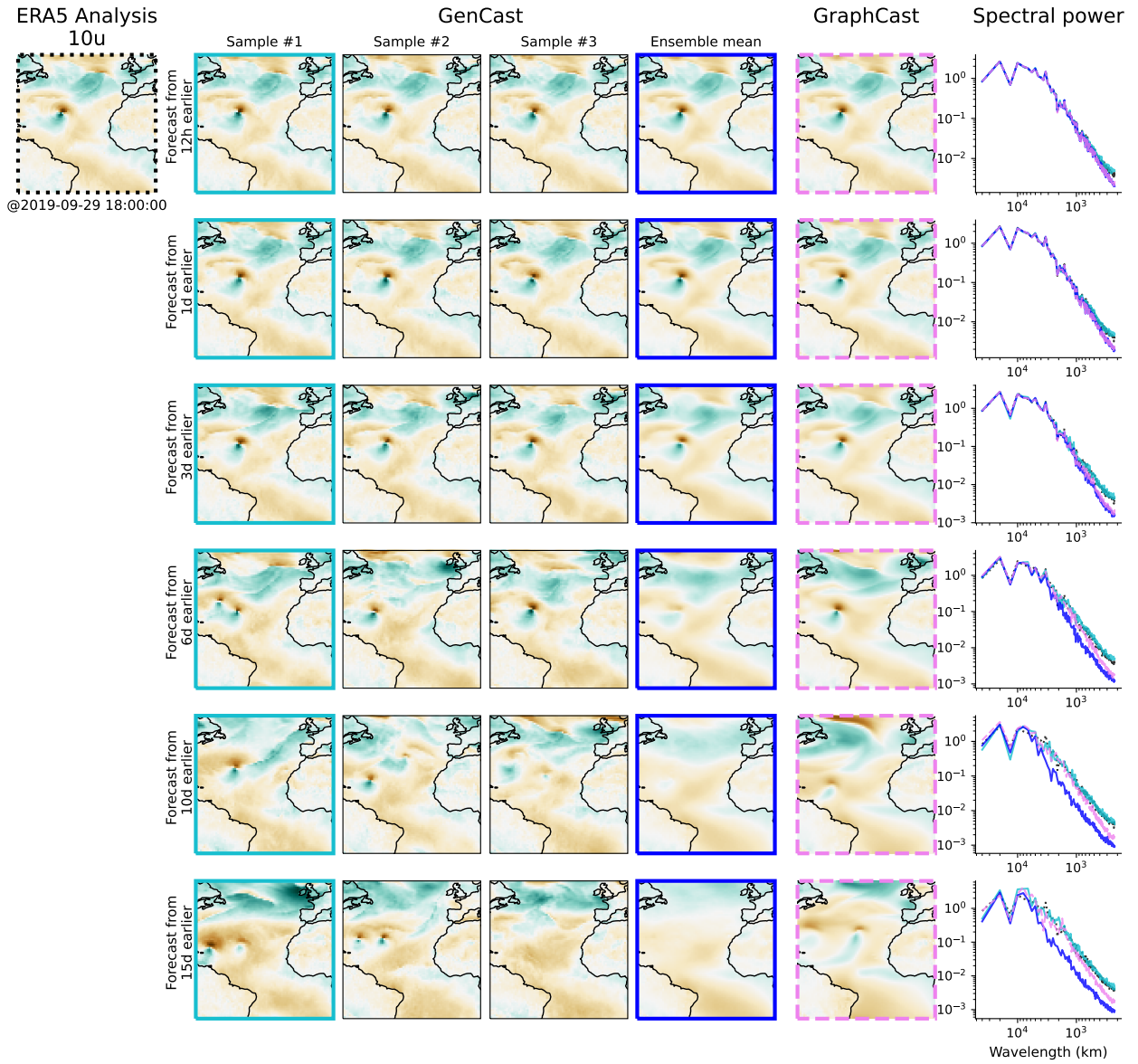


Figure A.20 | Visualization of 10u.

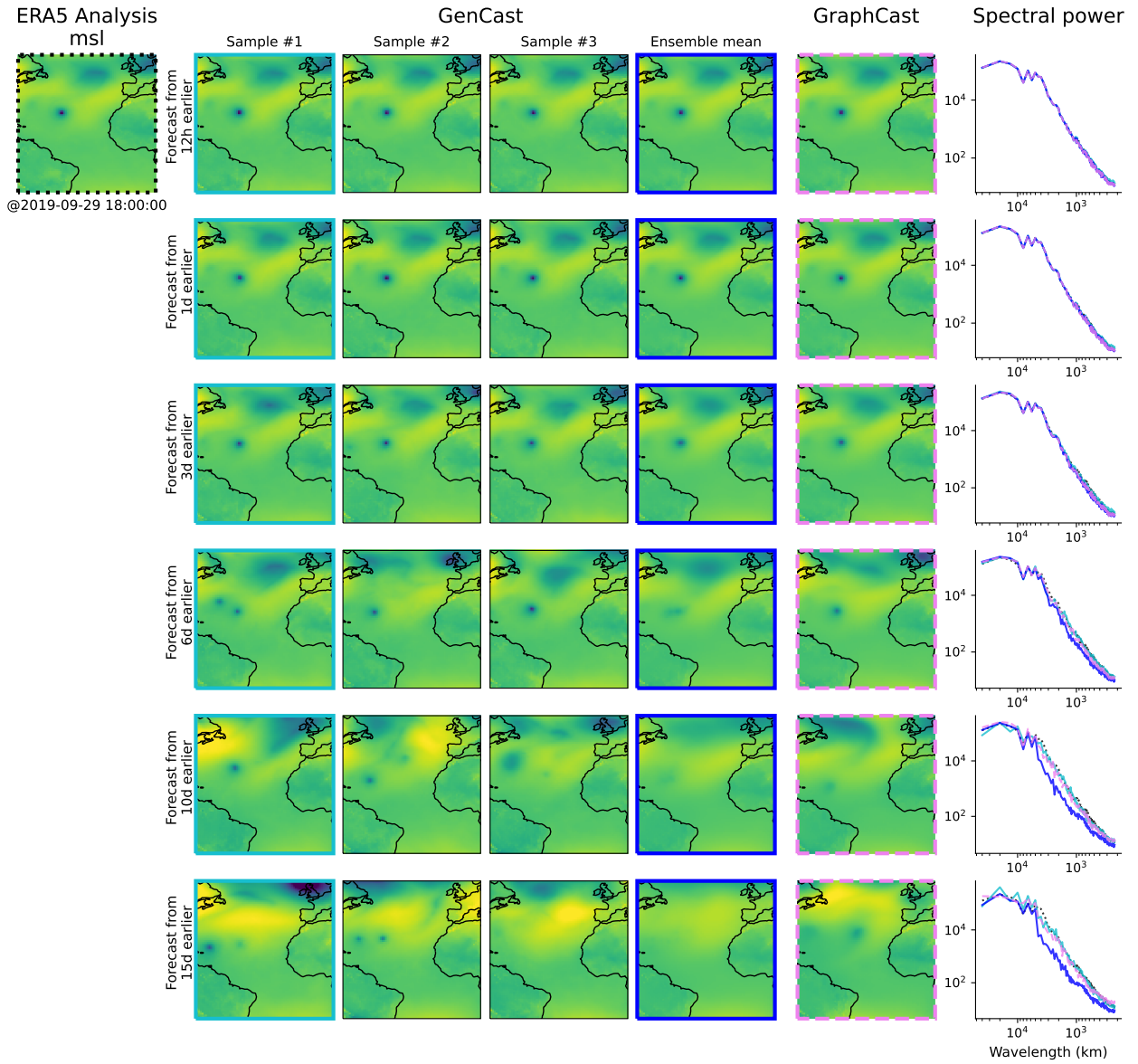


Figure A.21 | Visualization of msl.